

Materials Testing for Heatshield Applications during CubeSat Re-entry with Passive Demise

Claudio Vestini, Fizza Naqvi, Hani Moussa, Alex Berresford

April 20, 2025

1 Introduction

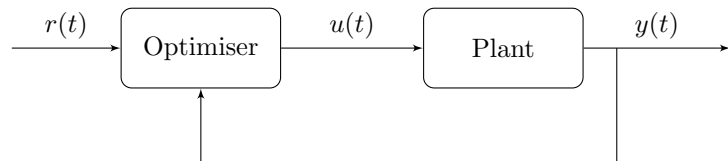
2 Trajectory

2.1 Attitude Control - Claudio Vestini

Attitude controller is a MIMO Model Predictive Control (MPC) implementation of a system with kinematics and dynamics, respectively (using quaternion representation):

$$\dot{q} = \frac{1}{2}\Omega(\omega)q; \quad J\dot{\omega} = -\omega \times (J\omega) + \tau$$

Knowledge of attitude state $y(t) \leftarrow q(t)$ is coupled with an Open-Loop altitude controller (cold gas thruster valve)



Attitude controller is a MIMO Model Predictive Control (MPC) implementation of a system with kinematics and dynamics:

$$\dot{q} = \frac{1}{2}\Omega(\omega)q; \quad J\dot{\omega} = -\omega \times (J\omega) + \tau$$

- $\omega \in \mathbb{R}^3$ is the angular velocity vector of the CubeSat wrt an inertial frame, expressed in the CubeSat's frame of reference

- $q \in \mathbb{R}^4$ is the quaternion attitude: $q := \begin{bmatrix} \eta \\ \epsilon \end{bmatrix} : \eta^2 + \|\epsilon\|^2 = 1$

- $\Omega(\omega) \in \mathbb{R}^{4 \times 4}$ is the skew-symmetric quaternion representation of angular velocity: $\Omega := \begin{bmatrix} 0 & -\omega_i & -\omega_j & -\omega_k \\ \omega_i & 0 & \omega_k & -\omega_j \\ \omega_j & -\omega_k & 0 & \omega_i \\ \omega_k & \omega_j & -\omega_i & 0 \end{bmatrix}$

- $J \in \mathbb{R}^{3 \times 3}$ is the moment of inertia matrix,

- $\tau \in \mathbb{R}^3$ is the applied torque: $\tau = \tau_a + \tau_d$ where τ_a is the actuator torque and τ_d is the disturbance torque.

Given unit quaternion:

$$\mathbf{q} = \eta + \epsilon_i \mathbf{i} + \epsilon_j \mathbf{j} + \epsilon_k \mathbf{k} \equiv \cos(\eta) (\epsilon_i \mathbf{i} + \epsilon_j \mathbf{j} + \epsilon_k \mathbf{k})$$

Any rigid body rotation can be represented as:

$$\mathbf{p}' = \mathbf{q} \mathbf{p} \bar{\mathbf{q}}$$

where η is the half-angle of rotation, and ϵ defines the rotation axis.

For constant angular velocity $\omega(t) = \omega_0$, the state update simplifies to:

$$\mathbf{q}(t) = \exp \left[\frac{1}{2} \Omega(\omega_0) t \right] \mathbf{q}(0)$$

3 Mechanical and Structural Design

4 Electronics

5 Aerothermal Environment

5.1 Introduction - Claudio Vestini

Since the first successful deployment of a human-made object into Earth's orbit with Sputnik in 1957, over 10,000 satellites have been placed in orbit around our planet [1]. Of these, over 84% are in low Earth orbit (LEO), of which only a relatively small percentage are still operational. This increasing accumulation of orbital space debris poses a significant threat to current and future space missions, which has led to a growing emphasis on effective end-of-life disposal strategies for spacecraft and ground impact mitigation techniques after their demise. To this scope, the European Space Agency (ESA) issued a report in 2014 [2] (later revised in 2023 [3]) that ordered the casualty risk for any re-entry event should be no greater than 1 in 10,000. Several other space agencies, including NASA, the Inter-Agency Space Debris Coordination Committee (IADC) [4] and the European Space Agency (ESA) [5], also agree with the prescription.

Accurately assessing casualty risk requires detailed understanding of fragmentation dynamics, surviving component geometries, impact locations, and geographical population density. One of the main sources of uncertainty in these assessments is the prediction of aerothermal heating during early re-entry stages. Unlike typical vehicles designed for re-entry, satellites often feature geometric discontinuities such as sharp edges and facets. This results in unique flow behaviours - particularly around corners - leading to increased local heat fluxes due to boundary layer thinning caused by strong expansions. This is a ripe field of research, as there is great concern associated with the Kessler syndrome [6]: in short, a scenario where the density of debris in Earth orbit is such that catastrophic collisions are inevitable. Existing demise prediction tools adopt various approaches in simulating these re-entry conditions: object-oriented tools like ORSAT and DRAMA use tumble-averaged heating rates for basic shapes [7, 8], while spacecraft-oriented models like SCARAB relate stagnation-point heating to a characteristic radius of curvature [9]. Newer tools such as FOSTRAD and PAMPERO employ local radius-of-curvature methods [10, 11]. None of these tools, however, relies on high-fidelity data for hypersonic aerothermal flow distributions around complex geometries, and a scarce number of studies and literature are available on the topic.

The AeroThermal team's overarching goal is to ensure CubeSat's thermal environment allows for the correct functioning of all electronics, telemetry, and control systems throughout our mission's phases, and to reliably guarantee the (sufficiently) complete demise of the satellite. The focus in this section of the report is the study of thermal environments to iteratively design CubeSats for commercial materials' testing, with emphasis on high-fidelity computational simulations of the heat fluxes and temperature distributions around the CubeSat throughout our mission. Thermal simulations of this kind inherently carry several layers of complexity. We simplified the analysis by separating simulations into two mission sections: the orbital (5.2), and the re-entry (5.3) phase. The stark differences in aerothermal environment dictate this decision: in orbit, the dominant thermal loading is that of incoming radiation from the Sun, whereas, during re-entry, the thermal environment is dominated by the dissipation of the kinetic energy of the hypersonic flow of air around the CubeSat [12].

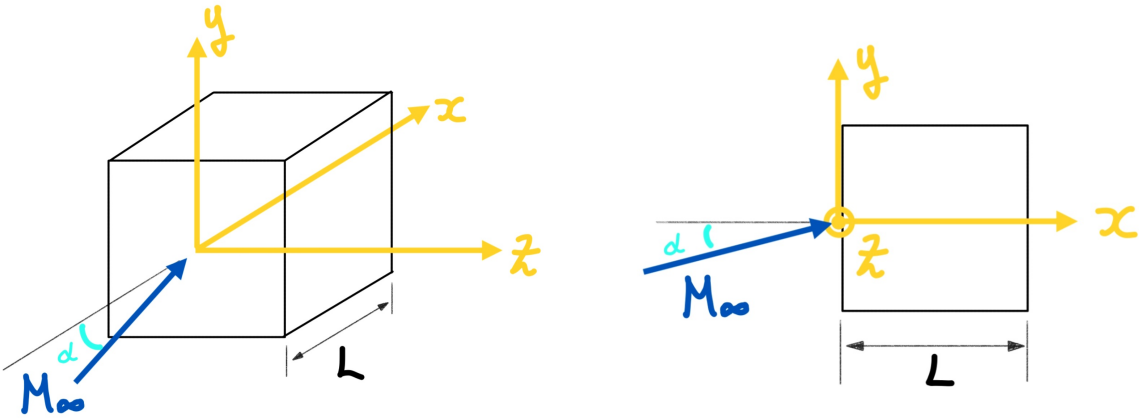


Figure 1: 3D (left) coordinate system for the CubeSat, where $L = 0.2$ m (8U). A slice through the centre of the cube reveals the 2D (x, y) coordinate system (right), where z is the depth variable into the walls. $M_\infty := \frac{v_\infty}{a}$, with $a = \sqrt{\gamma R T_\infty}$ [m s^{-1}], is the free-stream Mach number, and α is the in-xy-plane incidence.

Finally, we discuss the demise plan we established for our CubeSat mission. Given the adoption of ablative materials, the passive demise altitude of the CubeSat cannot easily be predicted. To significantly lower the probability of ground impact, we adopted Thermites to ensure complete demise is achieved (section 5.5). Given the nature of our product (a commercial materials testing platform), the aerothermal analysis must be iterated for every choice of heatshield configuration, based on the customer's material choices.

5.2 Orbital Phase - Claudio Vestini

5.2.1 Heat Equation and Geometry

The three-dimensional, convection-less, unsteady heat equation with internal heat generation is given by:

$$\frac{1}{\alpha} \frac{\partial T}{\partial t} = \nabla^2 T + \frac{G}{k} \quad (1)$$

where:

- $T(\mathbf{x}, t)$ is the scalar temperature field over the CubeSat's walls, with units [K],
- k is the material's thermal conductivity, with units [W m^{-1}]
- α is the thermal diffusivity, given by $\alpha = \frac{k}{\rho c_p}$, where ρ is material density and c_p is specific heat capacity, and has units [$\text{m}^2 \text{s}^{-1}$]
- $G(\mathbf{x}, t)$ is the volumetric rate of internal heat generation, with units [W m^{-3}]

The reference coordinate system adopted for this analysis is shown in Figure 1.

5.2.2 Flight Configuration and Assumptions

A sketch of relevant aerothermal factors during the orbital phase of our mission is shown in Figure 2.

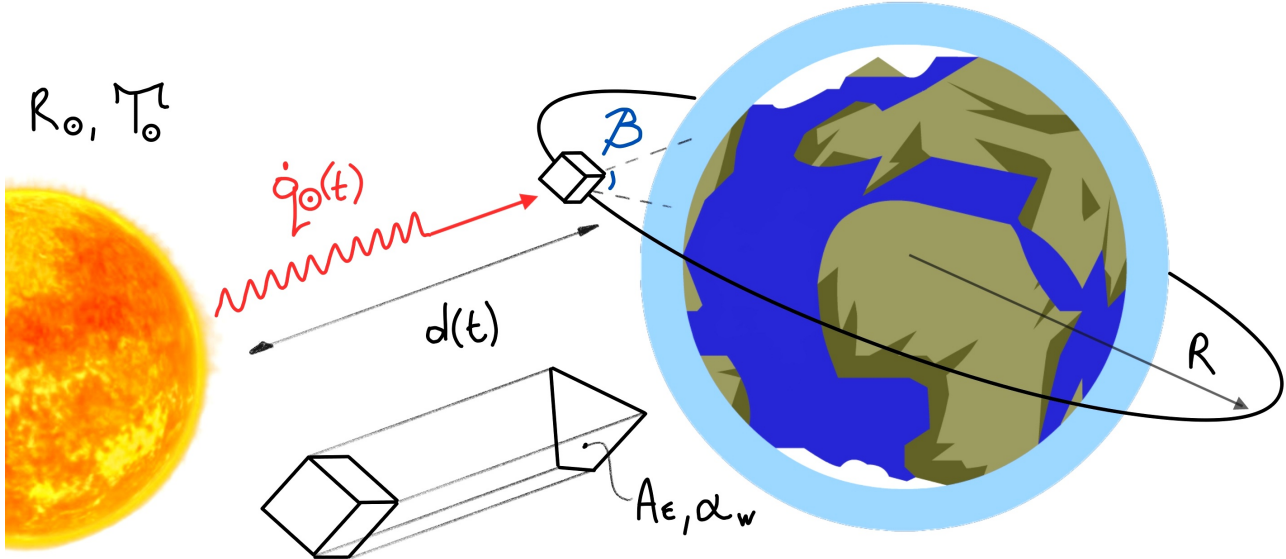


Figure 2: A sketch of CubeSat in orbit around the earth, with incoming radiation intensity $\dot{q}_\odot(t)$ [W m^{-2}] (at the CubeSat's surface). R_\odot and T_\odot are sun's radius [m] and surface temperature [K], respectively, whereas R is the orbital radius measured from the centre of the earth; that is: $R = R_e + R_{\text{orbit}}$. The sun-to-CubeSat distance is $d(t)$ [m], and β is the angle between a satellite's orbital plane around Earth and the geocentric position of the Sun. A_E is the effective thermal area of the CubeSat (geometric property), and α_w is the absorptivity of the outer walls (material property).

To estimate the surface temperature distribution $T(x, y, z = 0, t)$, we make the following assumptions:

- The orbital period can be divided into two sections: when CubeSat is wetted by incoming sunlight, and when CubeSat is behind Earth's shadow. The percentage of time spent in the shadow part of the orbit is given by illumination ratio $f_e := \tau_{\text{shadow}}/\tau_{\text{orbit}}$.
- The orbital period τ_{orbit} is much greater than the time taken for the CubeSat to transition behind Earth's shadow. This is justified as the dimensions of the CubeSat are negligible compared to those of the Earth, and the CubeSat travels at high velocity.
- The surface temperature of the sun is constant¹ at $T_\odot = 5772$ K, and its radius is $R_\odot = 6.9634 \times 10^8$ m.
- The distance d can be assumed to be constant. This is because $d(t) = d_0 + \delta d(t)$, with $d_0 = 1\text{AU}$ ² and $\max_t \delta d(t) = (R_e + R_{\text{orbit}})/\cos \beta \ll d_0$ (the maximum variation in distance δd_{max} is <0.001% of d_0).
- The effective thermal area A_E of the CubeSat is constant. It can be shown [13, 14] that, for any convex polyhedron illuminated by an infinitely-far-away light source, the average area of the shadow it casts on a two-dimensional plane is one-quarter of its surface area. Hence, for our CubeSat: $A_E = \frac{1}{4}(A_w)$.
- The effects of non-radiative heating factors (such as kinetic theory particle interactions) are negligible³.

With the above assumptions, the incoming radiation density $\dot{q}_\odot(t)$ is found to be a square wave with "OFF"

¹The Sun is considered a very stable star in terms of its energy output. Its total luminosity (total solar irradiance) varies by only about 0.1% throughout its 11-year solar activity cycle, justifying the assumption.

²1AU = $1.495978707 \times 10^{11}$ m

³In practice, thermal loading of an orbiting satellite from sources other than the sun can represent 15 % of the total, with trapped particles in Earth's magnetosphere being the dominant contributor [15]. However, a comprehensive analysis to include these location-dependent effects was deemed beyond the scope of this design exercise.

period equal to $f_e \tau_{orbit}$ and "ON" period $(1 - f_e) \tau_{orbit}$. The illumination ratio f_e is calculated [16] using:

$$f_e = \frac{1}{\pi} \cos^{-1} \left\{ \frac{\sqrt{R_{orbit}^2 + 2R_e R_{orbit}}}{(R_e + R_{orbit}) \cos \beta} \right\} \quad (2)$$

where $R_{orbit} = 400$ km is our orbital altitude and $R_e = 6371$ km is Earth's radius. Assuming β remains low for our orbit, $\cos \beta \approx 1 \implies f_e = 0.3898 \simeq 40\%$. The evolution of radiation intensity is plotted in Figure 3 (solid red line).

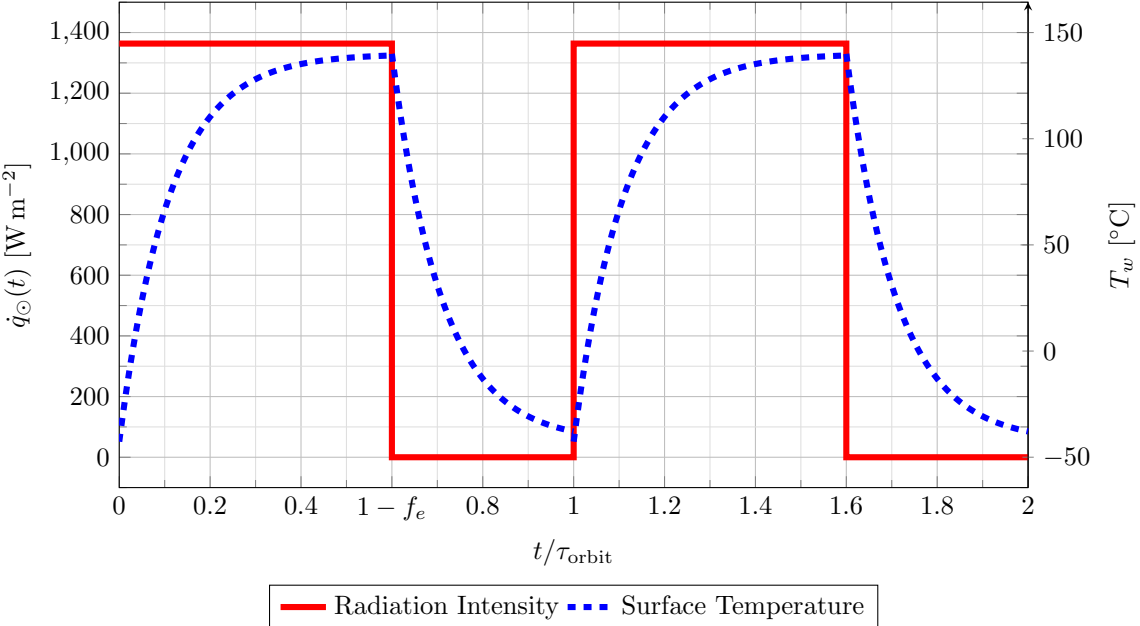


Figure 3: Plot of radiation intensity \dot{q}_\odot and surface temperature T_w evolution over dimensionless time. $t/\tau_{orbit} \in [0, 1 - f_e]$ represents the "ON" period (when CubeSat is directly illuminated), whereas $t/\tau_{orbit} \in (1 - f_e, 1]$ is the "OFF" period. The period Orbital period is $\tau_{orbit} \simeq 92.5$ min (as discussed in Section citeFIZZA), and max radiation intensity intensity is 1363.6 W m^{-2} . Surface temperature is found to oscillate between -42.7°C and 139.2°C (see Section 5.2.4).

To compute a worst-case lower bound for the wall temperature, we further assume no heat conduction through the CubeSat's wall during the "ON" period. Wall temperature during the "ON" period will therefore be uniform and constant: $T(x, y, z = 0, t) = T_w$. We recall the Stefan-Boltzmann law:

$$\dot{q}_r = \epsilon_r \sigma T^4 \quad (3)$$

where ϵ_r is the emissivity of the surface and σ is the Stefan-Boltzmann constant, with a value of $5.670374419 \times 10^{-8} \text{ [W m}^{-2} \text{ K}^{-4}\text{]}$. ϵ_r can range from 0 to 1, where $\epsilon_r = 1$ corresponds to a perfect black body (which we will assume for the sun). By Kirchhoff's law [17], emissivity ϵ_r and absorptivity α_r are equal for any thermal surface.

5.2.3 Boundary Conditions

The heat intensity at the satellite will depend on the view factor between the two bodies, given by $\frac{R_\odot}{d}$. Hence the incident heat intensity at the CubeSat's surface is given by $\dot{q}_\odot = \alpha_w \left(\frac{R_\odot}{d}\right)^2 (\epsilon_\odot \sigma T_\odot^4) \simeq 1363.6 \text{ W m}^{-2}$ (with black body assumption). During the "ON" period, the heat absorbed by the CubeSat must equal the heat it radiates away if no conduction occurs. A simple heat balance yields:

$$\dot{Q}_\odot = A_E \alpha_w \left(\frac{R_\odot}{d}\right)^2 (\epsilon_\odot \sigma T_\odot^4) = \dot{Q}_w = A_w \epsilon_w \sigma T_w^4 \quad (4)$$

Hence, the steady-state surface temperature will be:

$$T(x, y, z = 0, t) = T_w = T_\odot \sqrt{\epsilon_\odot \left(\frac{A_E}{A_w}\right) \left(\frac{\alpha_w}{\epsilon_w}\right)} \sqrt{\frac{R_\odot}{d}} \approx \frac{T_\odot}{2\sqrt{2}} \sqrt{\frac{R_\odot}{d}} \simeq 139.2^\circ\text{C}$$

We use this as an initial condition to predict the transient conduction behaviour during the "OFF" period.

5.2.4 IHCP Solver

With this initial condition, we estimate the surface heat flux experienced by a CubeSat during its orbital heating phase by solving an inverse heat conduction problem (IHCP). The "inverse" nature of this problem stems from the backwards nature of the calculation: to solve the heat equation *forwards*, we require a priori knowledge of heat fluxes, then solve for temperature distributions. In our case, we know the temperature distribution (it suffices to know the inner and outer temperatures). The IHCP is formulated and solved using a numerical finite difference scheme known as Forward-Time Central-Space (FTCS). The heat shield is modelled as a one-dimensional multilayered domain representing an ablative sandwich structure composed of distinct thermal protection layers, each with known thermal properties. It is discretised spatially into L total nodes across M material layers, each with thermal conductivity k_j , specific heat $c_{p,j}$, density ρ_j , and thickness L_j . Numerical schemes approximate the field variable of interest $\phi(x, t)$ as $\phi(x_l, t_n) \simeq \phi_l^n$ (in higher dimensions, there can be several spatial variables) by discretising the spatial and temporal domains as *stencil* (5). Differences between one scheme and another lie in the choice of the interpolating functions used.

$$(x_l, t_n) = (l\Delta x, n\Delta t); \quad (l, n) \in [0, (M - 1)] \times [0, (N - 1)] \in \mathbb{Z} \quad (5)$$

with domain bounds (x_F, t_F) , where l and n are discrete spatial and temporal indices, respectively, and $(\Delta x, \Delta t) = (x_F/(M - 1), t_F/(N - 1))$ are the domain step sizes. An important parameter to describe discretisation resolutions lies in the dimensionless Courant number $C := c \frac{\Delta t}{\Delta x}$, which represents the ratio between the distance travelled by a disturbance over a time step and the size of the grid spacing (c is the characteristic speed, equal to thermal diffusivity α for our case). A choice of m neighbouring points considered to approximate the differential operators gives rise to a $(m - 1)^{th}$ order scheme. This can be inferred from a direct comparison

with the solution's Taylor series expansion. FTCS is a suitable choice for the IHCP due to its simplicity, modularity, efficiency, and explicit nature. It has second-order accuracy in space and first-order accuracy in time. In our case, the variable of interest ϕ is scalar temperature T , and the governing equation (GE) is the unsteady, one-dimensional heat equation (1). Discretising the GE using the FTCS scheme yields:

$$\frac{T_l^{n+1} - T_l^n}{\Delta t} = \frac{1}{\rho_l c_{p,l} \Delta x_l} \left[k_{l+\frac{1}{2}} \frac{T_{l+1}^n - T_l^n}{\Delta x_{l+\frac{1}{2}}} - k_{l-\frac{1}{2}} \frac{T_l^n - T_{l-1}^n}{\Delta x_{l-\frac{1}{2}}} \right]. \quad (6)$$

To ensure conditional stability of the explicit scheme, the time step must satisfy the FTCS criterion for the most diffusive layer:

$$\Delta t \leq \min_j \frac{\Delta x_j^2}{2 \alpha_j}, \quad \alpha_j = \frac{k_j}{\rho_j c_{p,j}} \quad (7)$$

Re-arranging equation (6), for interior nodes $l = 1, \dots, M - 1$, the multilayer FTCS update of the temperature field T is:

$$T_l^{n+1} = T_l^n + \frac{\Delta t}{\rho_l c_{p,l} \Delta x_l} \left[k_{l+\frac{1}{2}} \frac{T_{l+1}^n - T_l^n}{\Delta x_{l+\frac{1}{2}}} - k_{l-\frac{1}{2}} \frac{T_l^n - T_{l-1}^n}{\Delta x_{l-\frac{1}{2}}} \right] \quad (8)$$

At the external surface node $l = 0$, the unknown inward heat flux q_0^n is imposed by

$$-k_{1/2} \frac{T_1^n - T_0^n}{\Delta x_{1/2}} = q_0^n \quad (9)$$

with $T_0 = T_w$, given above, while at the rear face $l = M - 1$ we enforce $T_{M-1}^n = T_{back}(t_n)$, assuming an initial internal wall temperature of $T_{back}(t_0) = 20^\circ\text{C}$. This assumption is justified as the conditions just after orbit insertion are analogous to those right before launch, and we can assume the CubeSat will be thermally insulated by the launch vehicle until insertion.

This scheme was implemented in a Python 3.11 codebase. The forward-time problem is solved repeatedly via the FTCS update (8)–(9). At each step, the new internal and external wall temperatures are updated as new boundary conditions. Temperature evolution T_l^n is used to reconstruct the surface flux history $\{q_0^n\}$. We note that no ablation effects are considered in the scheme. This is justified as the wall temperatures during this mission phase will not be anywhere close to the ablation onset thresholds.

Results for a typical (arbitrary) selection of wall material properties are $\max_n q_0^n = 433 \text{ W m}^{-2}$. The temperature evolution over two orbital periods is plotted in Figure 3 (blue dashed line). It shows "capacitor charging" behaviour during the "ON" orbital period, and "discharging" over the "OFF" period. This matches intuition; however, these results will have to be subject to future experimental validation.

5.3 Re-Entry Phase - Claudio Vestini

5.3.1 The Challenge of Hypersonic Flows

The aerothermal analysis for the re-entry phase is significantly more complex in nature. In general, very few simplifying assumptions can be made when analysing hypersonic flow regimes, and publicly available literature is limited to simple geometries such as spheres and flat-faced cylinders, which were extensively studied in the 1960s [18]. Often, aerodynamic and thermal correlations are taken from these geometries and adapted to more complicated flows, with fudge-factor corrections. In this analysis, we instead wish to directly predict the aerodynamic and thermal loadings of hypersonic flow regimes around a cube. Fluid simulation tools are standard in complex analyses like the one in question. However, these simulations are highly dependent on user choices of mesh geometries, solution formulations and methods, turbulence models, discretisation schemes, and boundary conditions. Poor engineering choices may result in inaccurate, yet precise and well-behaved predictions.

For hypersonic flow regimes, the challenge of obtaining accurate simulation predictions is enhanced: the presence of strong shocks resulting in thin shock layers, entropy layers which interact with viscous boundary layers, extreme flow temperatures behind normal shocks and the complex nonequilibrium thermochemical reactions [12, 19] are all complications that arise in continuum flow regimes. At high values of Knudsen number [20], defined as $\text{Kn} := \frac{\lambda}{L}$, where λ is molecular mean free path length and L is the characteristic physical length scale of the system (sidelength in this case), individual molecular kinetic interactions have to be considered, and the Continuum Model is no longer valid. In the limit of infinite Knudsen number, the regime is known as Free Molecular Flow (see Figure 4).

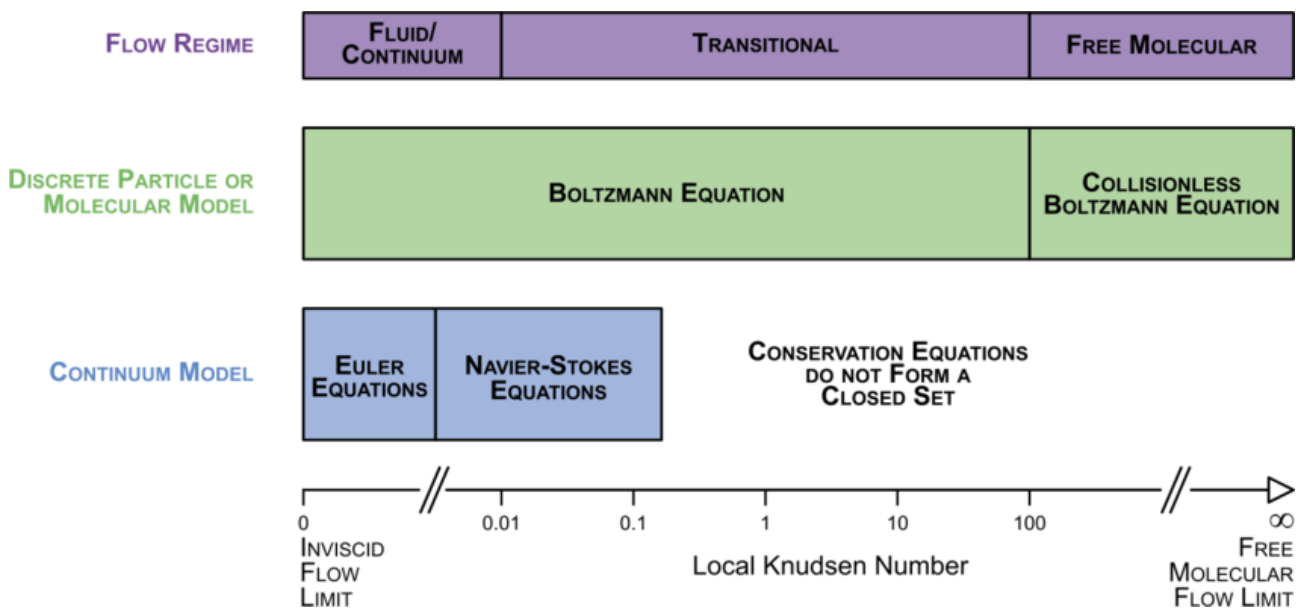


Figure 4: Illustration of flow regimes as a function of Knudsen number, as well as the intervals for which different models (continuum and discrete) are valid. Taken from Marschall et al. (2020), itself adapted from Bird (1994).

Hypersonic flow distinguishes itself from classical supersonic regimes chiefly due to the elevated temperatures reached in the shock layer behind strong shocks, which significantly alter the chemical composition of the gas. As the CubeSat re-enters through the atmosphere, stagnation temperatures can exceed 800 K, activating

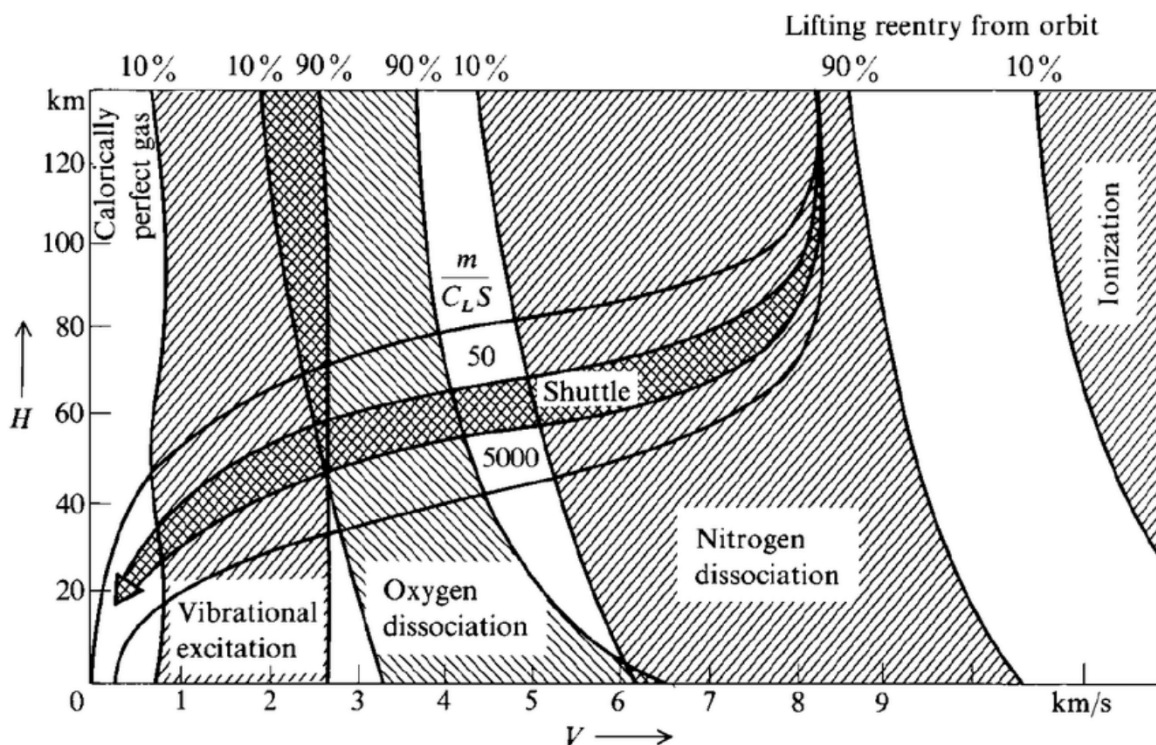


Figure 5: Thermochemical effects in hypersonic flow as a function of altitude and velocity during atmospheric re-entry. The diagram highlights the onset of vibrational excitation, oxygen and nitrogen dissociation, and ionisation, overlaid with typical re-entry trajectories such as that of the NASA Space Shuttle. Adopted from Anderson (2006).

vibrational modes in air molecules and leading to a temperature-dependent variation in specific heats [12]. At approximately 2000 K, these excitations become sufficiently energetic to dissociate molecular oxygen, and at 4000 K, the majority of O₂ has transitioned into its atomic form. These highly reactive atomic species initiate further thermochemical reactions, predominantly involving nitrogen and oxygen combinations. At even higher temperatures, nitrogen molecules (N₂) begin to dissociate. Due to the strong triple bond in N₂, this process requires more energy than the dissociation of oxygen and becomes significant above approximately 8000 K [12]. The resulting atomic nitrogen contributes to a dense set of reactions in the shock layer, forming additional species such as nitric oxide (NO) and further altering the thermal and chemical properties of the flow. These effects are especially relevant in the design of thermal protection systems, as the presence of atomic nitrogen increases the reactivity and overall energy content of the boundary layer (see Figure 5 for the full picture).

As temperatures continue to rise, ionisation processes become significant, producing free electrons and giving rise to plasma formation in the surrounding flow [12]. Concurrently, radiation effects from both the boundary and shock layers become non-negligible, with the capacity to cool the surrounding gas while heating the CubeSat's surface. These phenomena - along with the marked nonlinearity of thermodynamic properties at such temperatures - render classical ideal gas assumptions largely inadequate [12]. The pronounced thermal gradients near the front faces of the CubeSat introduce considerable entropy differences into the system, resulting in a significantly thickened boundary layer downstream. Additionally, in many hypersonic scenarios, the close proximity between the shock front and the body (thin shock layers) causes direct interactions between

the viscous boundary and the shock layers, further complicating both the physical structure of the flow and the associated thermochemical environments [12]. This is most relevant at angles of attack close to 45° , where the frontal shock is expected to be attached to the CubeSat's leading edge.

5.3.2 Flow Distributions for CubeSats

Schlieren experimental results are available in the literature for critical hypersonic flow configurations around cube shapes. These inform qualitative simulation validation, and are shown in Figure 6.

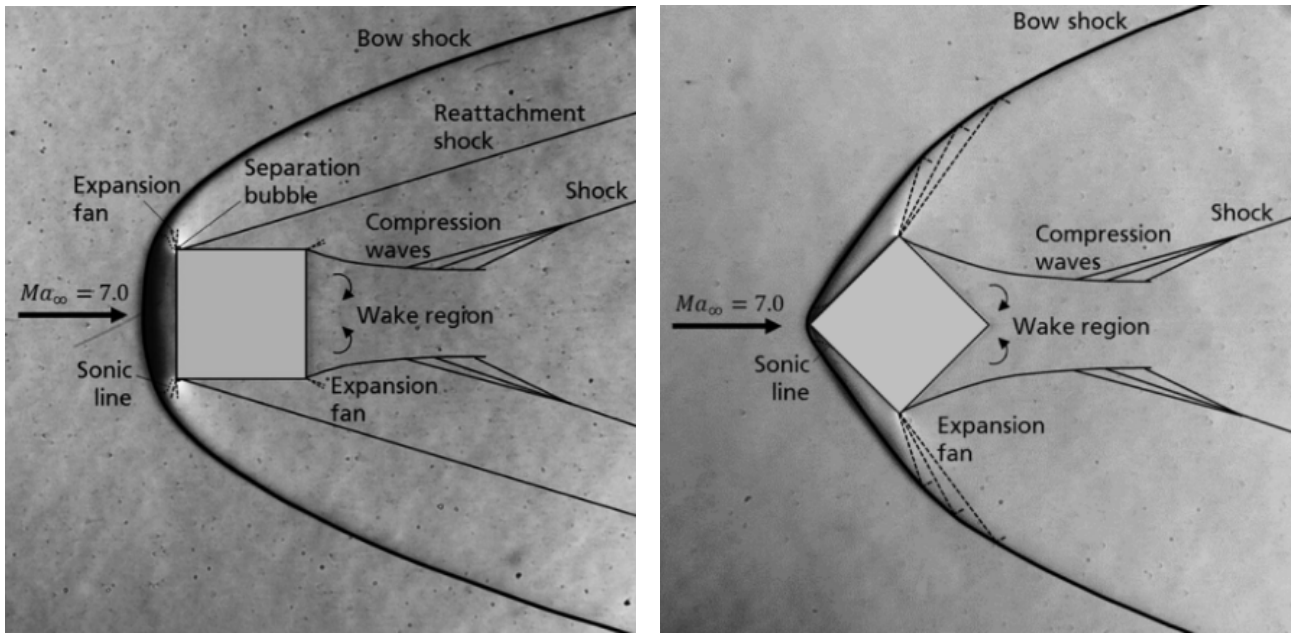


Figure 6: Critical flow configurations for a square in hypersonic flow, with $\alpha = 0^\circ$ incidence (left) and $\alpha = 45^\circ$ (right). Courtesy of Seltner, Willems, and Gühan (2019).

The flow patterns at zero incidence predictably show a detached bow shock forming ahead of the CubeSat. Behind this strong shock, an entropy layer wets the CubeSat's walls. The region just behind the shock will be subsonic, where temperatures are expected to reach their highest values. The flow then accelerates around the CubeSat's corners via strong Prandtl-Meyer expansions, forming a separation bubble. It was shown in [24] that the presence of the bubble is strongly dependent on Reynolds number but not Mach number, with separations forming for $Re > 5 \times 10^4$. The flow quickly reattaches to the top and bottom surfaces of the CubeSat through reattachment shocks. Not shown in 6 (left), a weak compression wave was found to form about halfway down the leeward edge of the CubeSat in [24]. Our simulations (see Section 5.3.3) also predict the existence of this Mach wave. The flow is then further expanded around the rear corners of the CubeSat, where a turbulent wake forms. At 45° incidence, the shock is attached to the stagnation corner of the CubeSat. With the absence of leeward-edge separations and reattachments, the rest of the flow field is similar in nature to the 0° incidence case.

5.3.3 CFD Simulations - Claudio Vestini

Computational Fluid Dynamics (CFD) has become an indispensable tool in the field of fluid mechanics, enabling engineers to perform preliminary studies of complex flow fields without the need for physical prototyping. CFD refers to the numerical solution of the governing equations of fluid flow, namely the Navier-Stokes equations. These represent mass, momentum, and energy conservation over a defined control volume. They are non-linear and coupled, requiring discretisation methods such as Finite Volume, Finite Difference, or Finite Element for non-elementary flow solutions:

$$\frac{\partial \rho}{\partial t} + \nabla \cdot (\rho \mathbf{V}) = 0 \quad (\text{Continuity}) \quad (10)$$

$$\frac{\partial(\rho \mathbf{V})}{\partial t} + \nabla \cdot (\rho \mathbf{V} \mathbf{V}^T + p \mathbf{I}) = \nabla \cdot \boldsymbol{\tau} \quad (\text{Momentum}) \quad (11)$$

$$\frac{\partial(\rho E)}{\partial t} + \nabla \cdot [(\rho E + p) \mathbf{V}] = \nabla \cdot (k \nabla T + \boldsymbol{\tau} \cdot \mathbf{V}) \quad (\text{Energy}) \quad (12)$$

Here, ρ is the fluid density, \mathbf{V} is the velocity vector, p is pressure, E is the total energy per unit mass, $\boldsymbol{\tau}$ is the viscous stress tensor, and k is thermal conductivity.

CFD simulation workflows can typically be broken down into:

1. **Geometry creation:** Internal or external flows to be studied, and CAD models can be imported.
2. **Mesh generation:** Most of the effort goes into this step.
3. **Solution setup and calculation:** Assignment of physical and computational models. Steady-state or transient solutions using residual-based convergence criteria (typical of high-fidelity simulations) or fixed-iteration runs (industry).
4. **Post-processing:** Results are analysed and visualised through plots.
5. **Verification and validation:** CFD solutions are often referred to as "garbage in - garbage out".

Validation against experimental results is arguably the most crucial step of the workflow, and often dictates the available choices of simulation conditions. The workflow, therefore, does not always follow the linear path described above. For hypersonic simulations of cubes, a limited number of research papers are available for validation. In particular, Rees analysed Stanton numbers for Mach 5 flows around a cube for small values of incidence in both 2D [24] and 3D [25] CFD simulations, which they validated against hypersonic wind tunnel experiments [26]. Seltner focused on aerodynamic coefficients and schlieren imaging of Mach 7 flows around a cube [23]. Our simulations were designed to reproduce the flow conditions of these two sets of experiments for validation.

5.3.4 ANSYS Fluent Solver - Claudio Vestini

We adopted ANSYS Fluent, a popular, commercially available integrated CFD software package, for the presented simulations. Fluent solves the two- or three-dimensional compressible Navier-Stokes equations using two primary approaches:

- **Pressure-based solver:** Originally developed for incompressible flows, extended through coupled algorithms for compressible regimes [27].
- **Density-based solver:** Traditional choice for high-speed flows, now generalised with Roe flux-difference splitting for broader applications. Adopted here as it can achieve convergence faster and with less computational expense for supersonic simulations.

Fluent employs the Finite Volume Method (FVM), which is particularly advantageous because of its ability to process complex, unstructured meshes⁴ [27].

The software offers a wide range of turbulence models, including RANS (Reynolds-Averaged Navier-Stokes) models such as Spalart–Allmaras, $k-\varepsilon$ and $k-\omega$ (BSL or SST), and hybrid RANS-LES (Large Eddy Simulation) approaches such as DES (Detached Eddy Simulation) and SAS (Scale-Adaptive Simulation). Additionally, Fluent supports boundary-layer transition models and is equipped with models for chemical reactions and thermal non-equilibrium, enabling complex simulations involving combustion and multiphase flows. Fluent provides various discretisation schemes for both spatial and temporal resolutions, including first- and second-order accurate methods. It offers both steady-state and transient solutions. The software also features a powerful built-in mesh adaptation module for mesh refinement (more in Section 5.3.6).

5.3.5 Simulation Parameters - Claudio Vestini

For the purpose of this report, two-dimensional, non-reacting compressible Navier-Stokes results are presented to match the conditions of [24, 25]. It is noted that, for these flow conditions, the maximum temperature recorded (behind the shock) did not exceed the 2000 K threshold for O₂ dissociation, which is a further justification for the choice of non-reacting physics. We adopted the $k-\omega$ SST (Shear Stress Transport) turbulence model, the industry standard for high-speed flows around sharp geometries. A common challenge for hypersonic simulations is the misalignment of the stencil with flow solutions. This effect can cause spurious vorticity and shock-wave deformations (a demonstration is shown in Figure 7, and an instance from our simulations is shown in Figure 8), and it is known as the Carbuncle Phenomenon [28]. The nature of this phenomenon is (notoriously) poorly understood, and several cures have been proposed [29, 30, 31]. We implemented the Advection Upstream Splitting Method (AUSM) implicit flux discretisation method with vector splitting and second-order spatial accuracy, which helps in preventing carbuncles. Gradients were computed following the Green-Gauss Cell-Based method. The simulations assume steady-state conditions (see 5.3.8). Convergence was judged on flow residuals falling below 10^{-4} for ≥ 50 iterations, in addition to Mass Flow Imbalance ($MFI := 100(m_{inlet} - m_{outlet})/m_{inlet}$)

⁴A mesh is said to be "unstructured" if its constituent polyhedra are not arranged in an orderly fashion.

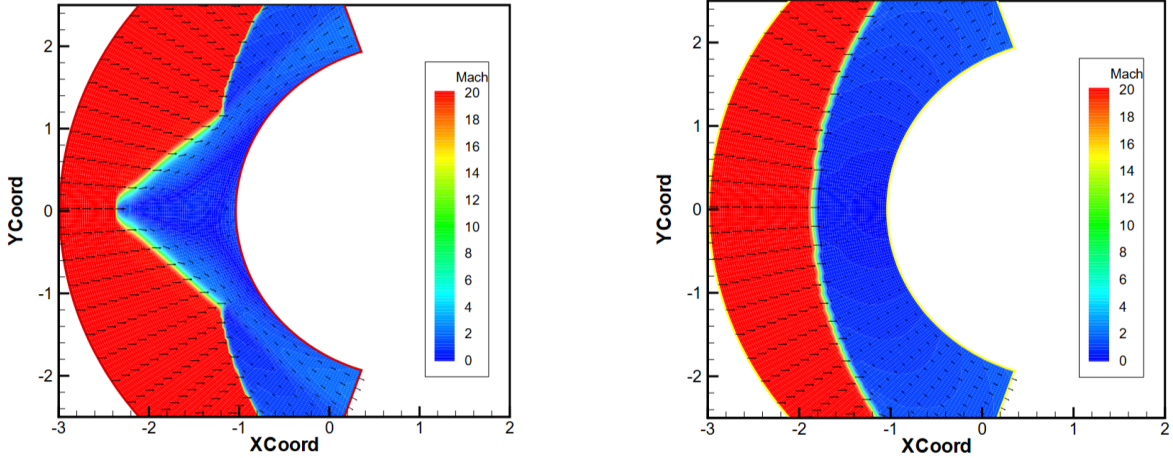


Figure 7: An illustration of the Carbuncle Phenomenon (left) compared to the stable solution for the same geometry (right). Figures from Ismail (2006).

falling below 2%. Future commercial simulations are to be run on a fixed-iteration basis.

5.3.6 Adaptive Mesh Refinement - Claudio Vestini

For our CubeSat simulation, we implement a simple square geometry of sidelength $L = 0.2$ m into a large rectangular domain of dimensions $5\text{ m} \times 10\text{ m}$. The large domain size allows for the application of far-field boundary conditions, and the capturing of wake effects downstream of the CubeSat. We are, however, compromising for computational cost. For this reason, and as good general CFD practice, mesh cell sizes are adapted to be finer close to walls (and shock-waves, more in Section 5.3.9), and coarser in the far-field. In addition, the cell shape is adapted to capture the steep gradients of boundary layers: a prismatic inflation layer is adopted near the four walls, where prevalent gradients are aligned in the wall-normal direction; polyhedral (triangular for the 2D case) cells are chosen away from walls for the remaining bulk of the fluid domain (see Figure 10).

To capture the effect of shocks and expansions, the position of such flow features must be known *a priori*. The practice of Adaptive Mesh Refinement (AMR) consists of computing the rough position of high-gradient features using unrefined meshes at first, then increasing cell counts in those locations where the highest gradients are located. This is visually explained in Figure 9.

5.3.7 Wall Treatment - Claudio Vestini

For high-speed external flows, turbulence modelling becomes critical due to the presence of shock-boundary layer interactions and laminar-to-turbulent transitions. In this study, particular attention was given to near-wall boundary layers, as their adequate resolution has a significant impact on temperature and heat flux distribution predictions. The dimensionless wall distance and velocity profile, y^+ and u^+ , respectively, are defined in terms of the friction velocity, u_τ , as:

$$u_\tau := \sqrt{\frac{\tau_w}{\rho}}; \quad y^+ := \frac{\rho u_\tau y}{\mu}; \quad u^+ := \frac{u}{u_\tau} \quad (13)$$

where y is the distance away from the wall, μ is the dynamic viscosity, ρ is fluid density and τ_w is the wall shear stress. In some CFD simulations involving turbulent boundary layers, it is a possible option to avoid simulating the boundary layer altogether. In this case, wall functions are used to bridge the near-wall region without fully resolving the viscous sublayer. For mesh designs relying on these standard wall functions, the first node should be placed within the logarithmic layer ($30 < y^+ < 300$). On the other hand, enhanced wall treatment models⁵ demand $y^+ \lesssim 1$ to resolve the viscous sublayer [32]. This is the type of simulation we are running. Fluent automatically adjusts wall function applicability based on local y^+ values and mesh density [27].

5.3.8 Boundary Conditions - Claudio Vestini

To simulate the aerothermal environment using CFDs, boundary conditions are required to fully establish the flow field. Throughout our CubeSat mission, far-field air density and composition, Mach and Reynolds numbers, flow incidence, pressure, and temperature will all vary continuously. There is consequently a vast spectrum of boundary conditions to be considered for testing. For commercial missions, the critical conditions (i.e. those that give the greatest aerothermal loadings) receive the highest level of scrutiny.

Given the nature of hypersonic atmospheric re-entry and our attitude control system, the CubeSat is expected to tumble throughout the mission at rates of $\Omega \approx 1 \text{ RPM}$ [**FIZZA**]. Since free-stream flow Mach numbers will be hypersonic for the entirety of the mission, the Strouhal number, defined as $\text{St} := \frac{\Omega L}{U_\infty}$ will remain very low: $\text{St} \lesssim 10^{-5}$. Hence, we can assume the flow field to always be fully developed in a quasi-steady state⁶. Transients can, therefore, be neglected, and the flow can be studied for a specific value of Mach and incidence. For the commercial application, a space of Mach versus α is to be populated to provide flow distributions for Mach values ranging from 25 to 5 and incidence angles ranging from 0° to 45° for each axis. This report will focus on simulations at Mach 5. The pressure and temperature boundary conditions to be presented were chosen as $P_\infty = 30\,000 \text{ Pa}$ and $T_\infty = 250 \text{ K}$ to represent typical static conditions at altitudes of about 50 km [33], which is predicted to be the rough location of maximum aerothermal loading. This is common for re-entry capsules, such as SpaceX's Dragon [34]. The simulation conditions have been summarised in Table 1.

Parameter	Variable Name	Run 1	Run 2	Run 3
Mach Number	M_∞	5	5	5
Velocity (m s^{-1})	U_∞	1177	1177	1584
Angle of Attack ($^\circ$)	α	0	45	0
Static Pressure (Pa)	P_∞	1584	1584	30000
Temperature (K)	T_∞	138	1338	250
Reynolds Number	Re_∞	72581	72581	7402939

Table 1: Summary of Boundary Conditions.

For a perfect gas, the relationship between the Mach number, Reynolds number, and Knudsen number is given by equation (14):

⁵Where the boundary layer is fully simulated

⁶Note that this assumption is very common for hypersonic re-entry simulations, as tumble rates are generally low compared to re-entry flow velocities.

$$\text{Kn} = \frac{M}{Re} \sqrt{\frac{\gamma\pi}{2}} \quad (14)$$

The regime of our simulations is therefore on the order of $\text{Kn} \sim 10^{-6}$, which lies within the range of the Continuum Model.

5.3.9 Mesh - Claudio Vestini

The mesh was generated using the ANSYS Workbench Meshing program, with geometry imported from ANSYS Discovery. A prismatic inflation layer was created with $\Delta y_{min} = 10^{-5}\text{m}$ for a total of 20 cells, and a moderate growth rate of 1.07 was selected. As a result, the value of y^+ was always below 1 within all four viscous sublayers. Additionally, the maximum value of the first cell Reynolds number, defined as:

$$Re_c = \frac{\rho_c a_c \Delta z}{\mu_c} \quad (15)$$

where ρ_c, a_c, μ_c are the local density, speed of sound, and viscosity of the fluid in the first cell, and Δz is the characteristic length scale of the cell (taken as the longest spatial dimension for structured meshes, or the cube root of cell volume for unstructured meshes), was recorded as 8.44. The first-cell Reynolds number serves as a standard criterion to ensure accurate prediction of surface heat flux, guaranteeing that flow gradients within the viscous boundary layer near the wall are properly resolved. Values of Re_c on the order of unity can reliably simulate heat transfer rates to the wall [35].

The mesh was also refined around the bow shock and expansions, as well as in the wake region, using an AMR routine with 4 meshes (coarse, medium, fine, and extra-fine) based on a Grid Convergence Index (GCI) defined as:

$$GCI_{ij} = \frac{S_F |\varepsilon_{ij}|}{r^p - 1}, \quad \varepsilon_{ij} = \phi_j - \phi_i, \quad i \in 1 : 3, \quad j = i + 1 \quad (16)$$

where the variable of interest ϕ_i was selected as Mach number on the stagnation streamline just ahead of the bow shock, $r = \Delta x_{coarse}/\Delta x_{fine} = 2$ is the refinement ratio, p is computed as $p = \ln(\varepsilon_{jk}/\varepsilon_{ij})/\ln r$ (with $k = j + 1$), and $S_F = 1.25$ is a safety factor. A GCI of 0.037 was obtained beyond the second refinement (comparing an eight-fold versus sixteen-fold finer mesh), confirming mesh independence across the bow shock for $i \geq 3$. The refinement study is illustrated in Figure 12, and the finalised mesh is shown in Figures 10, 11. We note that a similar re

5.3.10 Results - Claudio Vestini

Results for Mach number (with literature comparison for validation), static pressure and static temperature distribution contours are shown in Figures 13 and 14, respectively. A bow shock is found to form at 10.6 cm ahead of the leading edge. Other relevant flow structures are shown in Figure 16.

As shown in Figure 14 (left), static pressure is found to sharply rise above the far-field value behind the bow

shock, resulting in temperatures of upwards of 1510 K. A more detailed examination reveals that pressure values drastically drop behind the first set of strong Prandtl-Meyer corner expansions to a value of 6.18 kPa. As the flow is processed by the re-attachment shock, pressure rises to 17.2 kPa. As the flow recompresses, an adverse pressure gradient forms behind re-attachment location (pressure reaches 73.7 kPa just before the trailing edge), which is consistent with the findings of [24] section IV-C, in which it is stated: "the flow passes through the recompression wave and continues to compress until it expands over the leeward side of the square. The results suggest that the boundary layer has not recovered to its zero pressure gradient profile before expanding over the leeward surface of the square". Wake effects on pressure can be seen very faintly at the trailing edge in Figure 14 (left). Our simulation also predicts the formation of a weak compression wave about halfway down the leeward edge of the CubeSat, whose effects on static temperature can be seen clearly in Figure 14 (right).

Flow static temperature is seen to rise to values well above those behind the bow shock, and is greatest nearest the trailing edge corners, as shown in Figure 14 (right). We note that no analysis of the wake flow properties was provided in [24]; additionally, the wake was not included in the simulation of [25] (this can be seen in Figure 13 (left), where the picture displays the entire flow domain simulated). Due to this, the above analysis of wake distributions is tentative and kept brief. No further discussion of the wake is made within the rest of the report.

Figures ?? and ?? show distributions of temperatures, temperature gradients and heat transfer coefficients of the first mesh element along the leading and leeward edges, respectively. From Figure ??, we can see that static temperature spikes near the corners of the CubeSat. This behaviour is experimentally observed in [26], and shown in Figure 17. Our predicted maximum static temperature increase is $\Delta T_{\max} = 430$ K above a stagnation point temperature of $T_{\max} = 1510$ K. The CFD temperature prediction is larger than the experimental result by a factor of. This is due, in part, to the difference in static pressure conditions between the hypersonic wind tunnel discussed above. In addition, although the authors did not analyse temperature distributions in their 3D CFD simulations in [25] (their simulations were run with isothermal wall boundary conditions), they found sharp spikes in Stanton numbers near the four frontal corners, which were largely overpredicting the experimental result. This trend is reflected in our simulations. The leeward edge distribution of heat transfer coefficient shows good agreement with [25], where it was found to spike near the leading edge, and decay to values of 10% the stagnation point value. No validation data is available for temperature distributions on the leeward edge, so these predictions are only tentative. The wall-normal gradient near the corners is found to be orders of magnitude higher than the remaining distribution, and has therefore been omitted from the figure.

Figure 20 shows the wall-normal temperature distribution within the boundary layer along the leeward edge. These profiles closely follow the typical hypersonic boundary layer distribution, where static temperature rises above wall temperature, then decays to its free-stream value (see [12] chapter 1.3-C). The maximum temperature within the boundary layer is found to occur at $x = 3$ cm away from the leading edge, or right after flow compression.

5.4 IHCP Solver - Claudio Vestini

5.5 Thermite for Demise (T4D) - Claudio Vestini

Design-for-Demise (D4D) is a rapidly emerging field of study within aerospace engineering, which focuses on intentionally designing spacecraft to minimise the chance of ground impact through atmospheric re-entry. Within the spectrum of D4D methodologies, one particularly innovative approach is Thermite-for-Demise (T4D), which has been the subject of recent investigations at the *Politecnico di Milano* [36]. This strategy involves incorporating an additional source of enthalpy on board the spacecraft in the form of a thermite pyrotechnic charge, which is designed to passively ignite during the re-entry process. Thermites are a subset of energetic materials, typically composed of a metal and a metal oxide in powder form, which undergo an exothermic oxidation-reduction reaction upon ignition, releasing a significant amount of heat. These materials are attractive for space applications due to their high energy density and relative stability, as well as the possibility of selecting formulations that are relatively insensitive to external stimuli and non-toxic. Furthermore, the ignition temperature of thermites can be altered through formulation and processing techniques such as mechanical activation [37], where the powder is milled to alter its shape, granulometry, and surface finishing, resulting in tailored and predictable ignition characteristics.

The potential benefits of T4D are manifold. The additional heat released by the ignited thermite can aid the spacecraft in completing its demise by promoting ablation of robust components that might otherwise survive re-entry. This extra heat source can be strategically placed in the structural voids of particularly resilient components to specifically target their demise. Furthermore, the action of thermites can be employed to induce controlled fragmentation of the spacecraft, weakening structural joints and thereby increasing the overall surface area exposed to the intense aerothermal heating encountered during re-entry.

The Politecnico team conducted experiments to quantify the heat transfer efficiency between an ignited thermite powder and its confining vessel. In [38], an Al+Fe₂O₃ thermite mixture was confined in a cylindrical steel vessel and heated externally. The average heat transfer efficiency was found to be around 60% of the theoretical heat release. This efficiency was found to be significantly influenced by the geometry of the vessel: confined configurations eliminated convective and radiative losses, leading to higher efficiency compared to unconfined setups. The team also developed a numerical model called TRANSIT (TRAnsatmosferic SImulation Tool), to simulate the re-entry process with the inclusion of a thermite charge [36]. TRANSIT is an object-oriented tool that considers flight dynamics, aerothermodynamics, and heat transfer processes. It has been verified against commercial software packages like SAM and SCARAB [36]. TRANSIT allows for the preliminary sizing of the thermite charge by considering factors such as the mass ratio between the thermite and the spacecraft, the material reactivity, the heat release profile, and the total enthalpy release. Genetic algorithms are employed to optimise these parameters to ensure complete demise while minimising the required thermite mass [36].

For our project, the CubeSat undergoes atmospheric re-entry to evaluate the performance of ablative materials for heat shield purposes. The presence of an ablative heat shield, while crucial for protecting the payload

and enabling quantitative testing, will delay the complete disintegration of the CubeSat structure during the uncontrolled re-entry, thereby increasing the ground casualty risk. Consequently, the implementation of T4D presents a compelling strategy to ensure complete demise upon re-entry for our mission. To minimise the probability of ground impact, we strategically implement a T4D system to provide a localised and intense internal heat source that works in conjunction with the external aerothermal heating.

In our final CubeSat design, the Thermite-for-Demise (T4D) system is implemented as an integrated solution with the rest of the assembly to ensure complete demise during atmospheric re-entry in the presence of ablative heat shielding. No electronics are required for ignition, as the heat loads are expected to be sufficient to activate the charges. Thermite charges are embedded within the most robust internal components, such as the electronics mounting structures, the three reaction wheel motors, and other dense mechanical elements expected to withstand the initial re-entry heating. Upon activation, these charges deliver intense, localised heating directly to the core of these components, promoting rapid melting and structural failure. Additionally, thermite charges are positioned at key structural joints within the CubeSat frame. This arrangement is designed to induce targeted weakening and controlled fragmentation of the structure during re-entry, thereby increasing the surface area-to-mass ratio of the debris and enhancing the likelihood of complete ablation in the upper atmosphere. To address the risk of residual protection from the ablative layer, the remaining thermite charges are located adjacent to the inner surface of the heat shield. These charges are configured to activate during the later stages of re-entry, breaching any remaining ablative material and exposing the underlying structure to direct aerothermal heating. This comprehensive T4D implementation ensures that the CubeSat does not survive re-entry in large fragments, thereby reducing the risk of ground casualties and fully aligning with current best practice in space debris mitigation.

The successful implementation of T4D in our CubeSat design requires optimisation of thermite formulation mass, placement geometry, and ignition triggering. Passive ignition via aerothermal heating remains the preferred activation method, necessitating thermites with tailored ignition temperatures to overcome the ablative shield's thermal buffering. The choice falls on a mechanically activated Al-Fe₂O₃ formulation, with ignition thresholds reduced to 450–600 K. Heat transfer efficiency from reacting thermite to structural components, quantified experimentally at ~60% in confined configurations [38], should be validated for our topology prior to launch.

Future work will further refine estimates using parametric studies in the TRANSIT tool. This tool's re-entry predictions will be cross-validated against SCARAB's established fragmentation models [40] to ensure robustness. Future experimental work should arc-jet test representative CubeSat segments with integrated thermite charges under representative heating profiles (3–5 MW/m² for 60–90 seconds), correlating demise progression with modelled predictions. These steps will advance the T4D methodology's maturity while ensuring compliance with ESA's 1:10,000 casualty risk threshold [2], establishing a framework for scalable materials testing missions within our platform.

References

- [1] NanoAvionics. *How Many Satellites are in Space?* Accessed: 2025-04-20. 2023. URL: <https://nanoavionics.com/blog/how-many-satellites-are-in-space/>.
- [2] Anon. *Space Debris Mitigation Policy for Agency Projects*. Tech. rep. ESA/ADMIN/IPOL(2014)2. ESA Director General's Office, 2014.
- [3] AA. VV. *ESA Space Debris Mitigation Requirements*. Tech. rep. ESSB-ST-U-007. European Space Agency, 2023.
- [4] AA. VV. *IADC Space Debris Mitigation Guidelines*. 2020.
- [5] AA. VV. *ESA's Annual Space Environment Report*. Darmstadt, Germany, 2022.
- [6] Donald J. Kessler and Burton G. Cour-Palais. "COLLISION FREQUENCY OF ARTIFICIAL SATELLITES: THE CREATION OF A DEBRIS BELT." In: *J Geophys Res* 83 (A6 1978), pp. 2637–2646. ISSN: 0148-0227. DOI: [10.1029/JA083iA06p02637](https://doi.org/10.1029/JA083iA06p02637).
- [7] J. Dobarco-Otero et al. "The Object Reentry Survival Analysis Tool (ORSAT) Version 6.0 and Its Application to Spacecraft Entry". In: *56th International Astronautical Congress*. Fukuoka, Japan, 2005.
- [8] C. Martin et al. *DRAMA Final Report*. Tech. rep. European Space Agency, 2005.
- [9] G. Koppenwallner et al. "SCARAB - A Multidisciplinary Code for Destruction Analysis of Spacecraft During Re-Entry". In: *5th European Symposium on Aerothermodynamics for Space Vehicles*. Cologne, Germany, 2005.
- [10] P. M. Mehta et al. "An Open-Source Hypersonic Aerodynamic and Aerothermodynamic Modeling Tool". In: *8th European Symposium on Aerothermodynamics for Space Vehicles*. 2015.
- [11] J. Annaloro et al. "Elaboration of a New Spacecraft-Oriented Tool: Pampero". In: *8th European Symposium on Aerothermodynamics for Space Vehicles*. 2015.
- [12] J.D. Anderson. *Hypersonic and High-temperature Gas Dynamics*. AIAA education series. American Institute of Aeronautics and Astronautics, 2006. ISBN: 9781563477805. URL: <https://books.google.com.sg/books?id=UgWmQgAACAAJ>.
- [13] Augustin-Louis Cauchy. "Note sur divers théorèmes relatifs à la rectification des courbes et à la quadrature des surfaces". French. In: *Comptes Rendus de l'Académie des Sciences* 13 (1841), pp. 1060–1065.
- [14] 3Blue1Brown. *A tale of two problem solvers — Average cube shadow area*. Accessed: 2025-03-24. 2021. URL: <https://www.youtube.com/watch?v=ltLUadnCyi0>.
- [15] Insoo Jun et al. "A review on radiation environment pathways to impacts: Radiation effects, relevant empirical environment models, and future needs". In: *Advances in Space Research* (2024). ISSN: 0273-1177. DOI: [10.1016/j.asr.2024.03.029](https://doi.org/10.1016/j.asr.2024.03.029). URL: <https://www.sciencedirect.com/science/article/pii/S0273117724003296>.

- [16] National Aeronautics and Space Administration. *LEO Satellite Illumination Analysis Report*. Technical Report NAS-2024-LEO-001. 2024. URL: <https://ntrs.nasa.gov/citations/20240001234> (visited on 03/24/2024).
- [17] Gustav Kirchhoff. “Über den Zusammenhang zwischen Emission und Absorption von Licht und Wärme”. In: *Monatsberichte der Königlich Preussischen Akademie der Wissenschaften zu Berlin* (1860), pp. 783–787.
- [18] Donald M. Kuehn. “Experimental and theoretical pressures on blunt cylinders for equilibrium and nonequilibrium air at hypersonic speeds”. In: *NASA Technical Report R-117* (1963).
- [19] Daniel F Potter. *Modelling of radiating shock layers for atmospheric entry at Earth and Mars*. 2011.
- [20] M. Knudsen. “Die Gesetze der Molekularströmung und der inneren Reibungsströmung der Gase durch Röhren”. In: *Annalen der Physik* 333.1 (1909), pp. 75–130. DOI: [10.1002/andp.19093330102](https://doi.org/10.1002/andp.19093330102).
- [21] Raphael Marschall et al. *Cometary Comae-Surface Links: The Physics of Gas and Dust from the Surface to a Spacecraft*. Dec. 2020. DOI: [10.1007/s11214-020-00744-0](https://doi.org/10.1007/s11214-020-00744-0).
- [22] G. A. Bird. *Molecular Gas Dynamics and the Direct Simulation of Gas Flows*. Vol. 42. The Oxford Engineering Science Series. Oxford: Clarendon Press, 1994. ISBN: 978-0-19-856195-8.
- [23] Patrick M. Seltner, Sebastian Willems, and Ali Gülan. “Aerodynamic coefficients of free-flying cubes in hypersonic flowfield”. In: *Journal of Spacecraft and Rockets* 56 (6 2019), pp. 1725–1734. ISSN: 15336794. DOI: [10.2514/1.A34345](https://doi.org/10.2514/1.A34345).
- [24] Thomas W. Rees, Paul J.K. Bruce, and James A. Merrifield. “The effect of reynolds number on the hypersonic flow around faceted shapes”. In: *22nd AIAA International Space Planes and Hypersonics Systems and Technologies Conference*. American Institute of Aeronautics and Astronautics Inc, AIAA, 2018. ISBN: 9781624105777. DOI: [10.2514/6.2018-5197](https://doi.org/10.2514/6.2018-5197).
- [25] Thomas W. Rees et al. “Numerical and experimental studies of the hypersonic flow around a cube at incidence”. In: *Acta Astronautica* 183 (June 2021), pp. 75–88. ISSN: 00945765. DOI: [10.1016/j.actaastro.2021.02.033](https://doi.org/10.1016/j.actaastro.2021.02.033).
- [26] Thomas W. Rees et al. “Experimental characterization of the hypersonic flow around a cuboid”. In: *Experiments in Fluids* 61 (7 July 2020). ISSN: 14321114. DOI: [10.1007/s00348-020-02975-x](https://doi.org/10.1007/s00348-020-02975-x).
- [27] David Bacci. *B19 Nozzle Flow Lab Notes: Introduction to CFD Best Practices*. Lab notes for B19 lab at the University of Oxford. 2025.
- [28] Farzad Ismail. *TOWARD A RELIABLE PREDICTION OF SHOCKS IN HYPERSONIC FLOW: RESOLVING CARBUNCLES WITH ENTROPY AND VORTICITY CONTROL*. 2006.
- [29] David I. Ketcheson and Manuel Quezada de Luna. “Numerical simulation and entropy dissipative cure of the carbuncle instability for the shallow water circular hydraulic jump”. In: *International Journal for Numerical Methods in Fluids* 93.7 (2021), pp. 2250–2267. DOI: [10.1002/fld.5070](https://doi.org/10.1002/fld.5070).

- [30] Simon Sangeeth and J. C. Mandal. "A cure for numerical shock instability in HLLC Riemann solver using antidiffusion control". In: *Computers & Fluids* 173 (2018), pp. 59–76. DOI: 10.1016/j.compfluid.2018.07.029.
- [31] J. M. Powers, J. Bruns, and A. Jemcov. "Physical Diffusion Cures the Carbuncle Phenomenon". In: *53rd AIAA Aerospace Sciences Meeting*. American Institute of Aeronautics and Astronautics. Kissimmee, Florida, 2015.
- [32] David C. Wilcox. *Turbulence Modeling for CFD*. 2nd. La Cañada Flintridge, CA, USA: DCW Industries, 1994.
- [33] ANSYS Inc. *Reentry Capsule Analysis Using ANSYS Fluent*. Accessed: 2025-04-07. 2025. URL: https://ansyshelp.ansys.com/Views/Secured/corp/v242/en/flu_tg/flu_tg_reentry_capsule.html.
- [34] Loretta Trevino. "SpaceX Dragon Re-Entry Vehicle: Aerodynamics and Aerothermodynamics with Application to Base Heat-Shield Design". In: *6th International Planetary Probe Workshop*. Discusses computational aerothermal analysis of Dragon capsule at Mach 2-21, with altitude-specific heating profiles. Atlanta, Georgia, USA, 2008, pp. 1–8. URL: <https://repository.gatech.edu/bitstreams/39f02e86-13a2-4066-a79d-2a87df7d2ccd/download>.
- [35] P.A. Gnoffo. "CFD Validation Studies for Hypersonic Flow Prediction". In: *Proceedings of the 39th Aerospace Sciences Conference*. Reno, NV, USA, 2001.
- [36] A. Finazzi et al. "Thermite-for-Demise Concept: from Material Selection to Test Campaign". In: *ESA-TRP SPADEXO project* (2024). Preprint.
- [37] S. Dossi et al. "Enhancing micrometric aluminum re-activity by mechanical activation". In: *Innovative Energetic Materials: Properties, Combustion Performance and Application*. Ed. by eds. Springer Nature, 2020, pp. 17–44. DOI: https://doi.org/10.1007/978-3-030-36426-3_2.
- [38] A. Finazzi et al. "Thermite-for-Demise (T4D): Experimental analysis of heat transfer principles and preliminary sizing of an application". In: *International Journal of Heat and Mass Transfer* 220 (2024), p. 124957. DOI: <https://doi.org/10.1016/j.ijheatmasstransfer.2023.124957>.
- [39] A. Finazzi et al. "Thermite-for-Demise (T4D): Experimental analysis of heat transfer principles and preliminary sizing of an application". In: *International Journal of Heat and Mass Transfer* 220 (Mar. 2024). ISSN: 00179310. DOI: 10.1016/j.ijheatmasstransfer.2023.124957.
- [40] G. Koppenwallner et al. "SCARAB - a multi-disciplinary code for destruction analysis of space-craft during re-entry". In: *5th European Symposium on Aerothermodynamics for Space Vehicles*. Cologne, Germany, 2005.

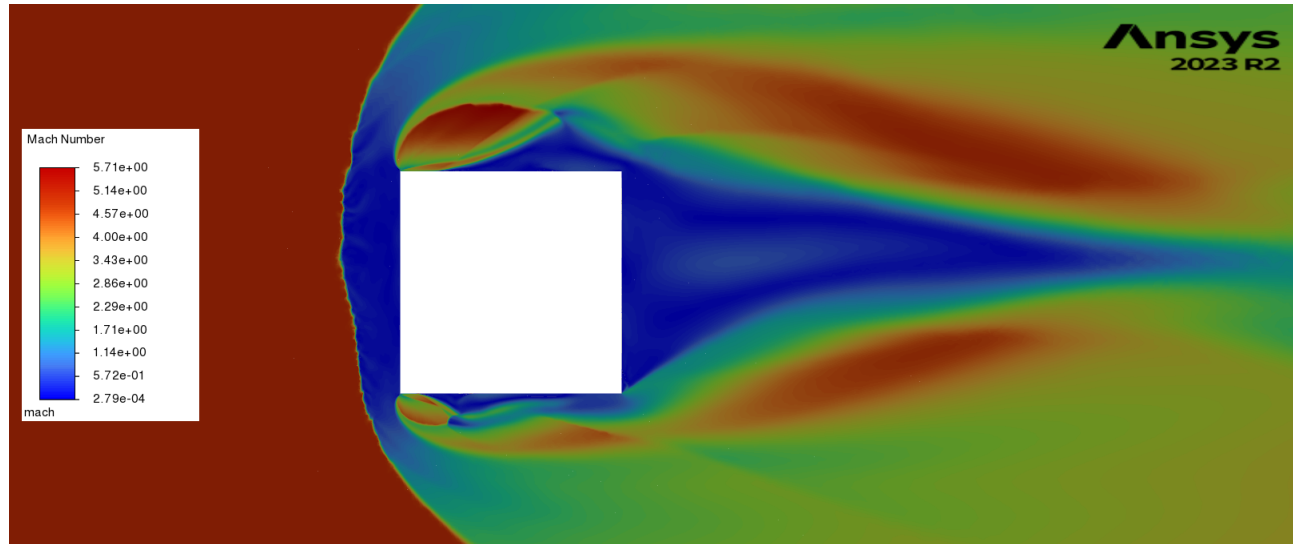


Figure 8: An instance of the carbuncle phenomenon. The plot shows contours of Mach number. It can be seen that the frontal shock behaves as if "punctured", and does not form a bow shape. It is also evident that this effect creates spurious asymmetries and nonphysical flow patterns after the shock.

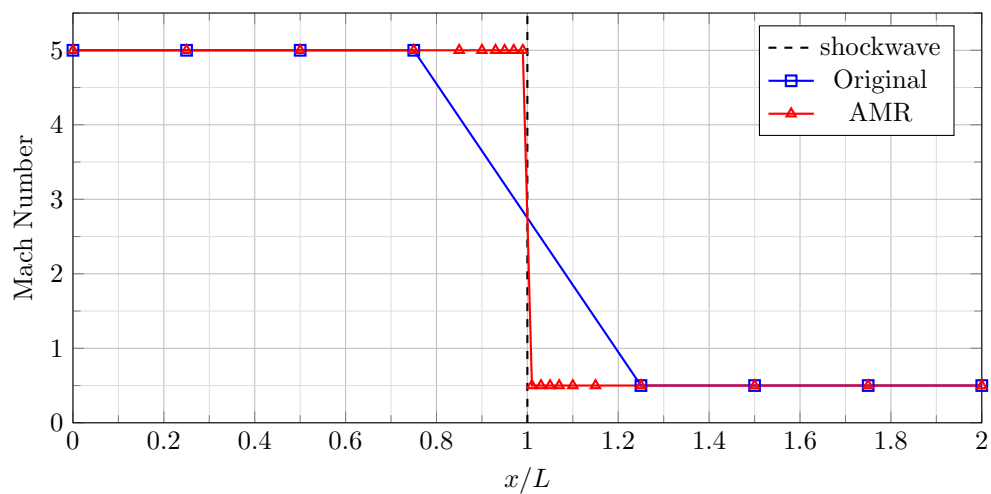


Figure 9: An idealised illustration of Adaptive Mesh Refinement for a normal shockwave at $x/L = 1$, with upstream Mach number of 5.0 and downstream Mach number of 0.5. The refined mesh (red line with triangle markers), with increased cell count near the high-gradient shock, provides a much better estimate of flow parameters.

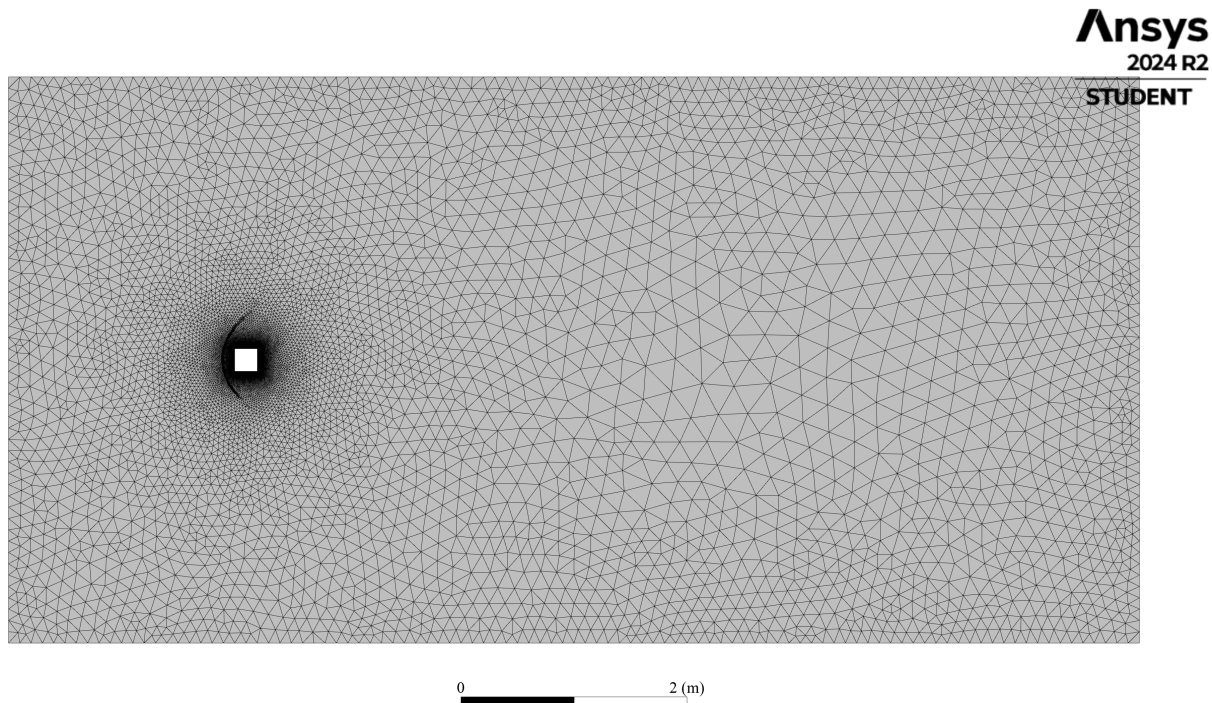


Figure 10: Domain Mesh for Run1. Fluid domain dimensions are $5\text{ m} \times 10\text{ m}$, and CubeSat dimensions are $0.02\text{ m} \times 0.02\text{ m}$. Mesh counts are 4.97×10^5 cells, 8.36×10^5 faces, and 3.34×10^5 nodes. Simulations were run on an ANSYS Professional license, but visualised in Post through a Student license.

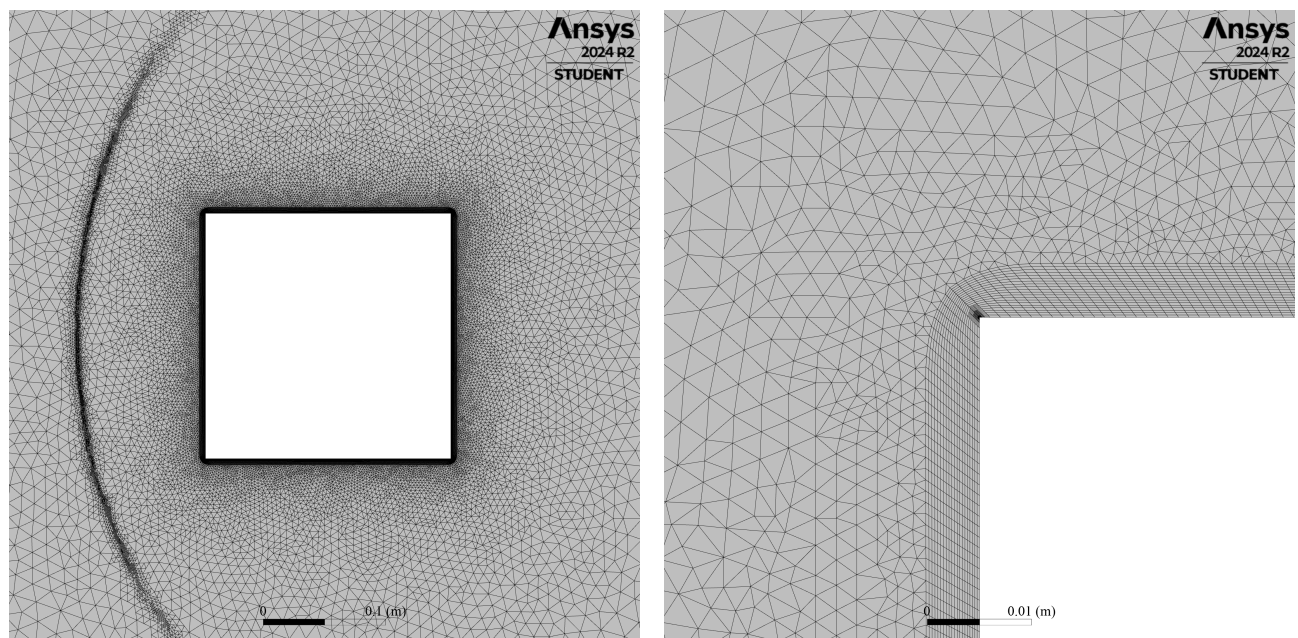


Figure 11: Detailed views of the CubeSat mesh for Run 1: Zoomed view (left) and corner detail (right).

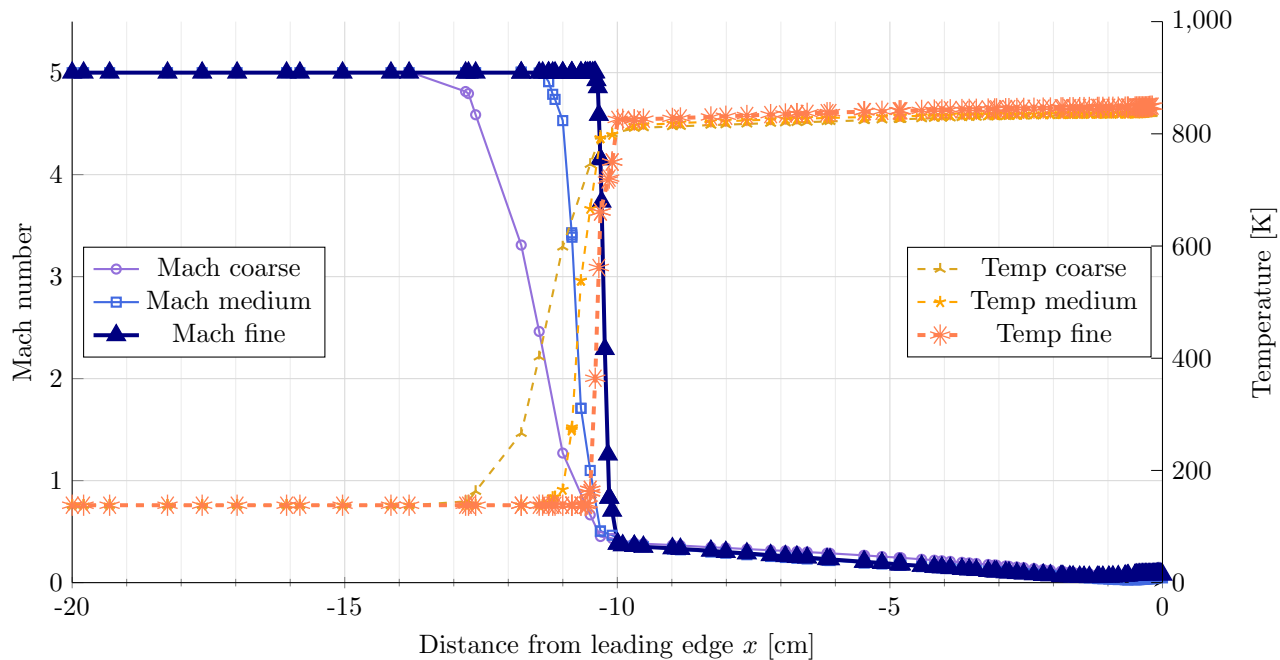


Figure 12: Mach number and static temperature profiles across the frontal bow shock on the stagnation streamline for different grid refinements. The final mesh refinement (fine) is shown with a thicker line width.

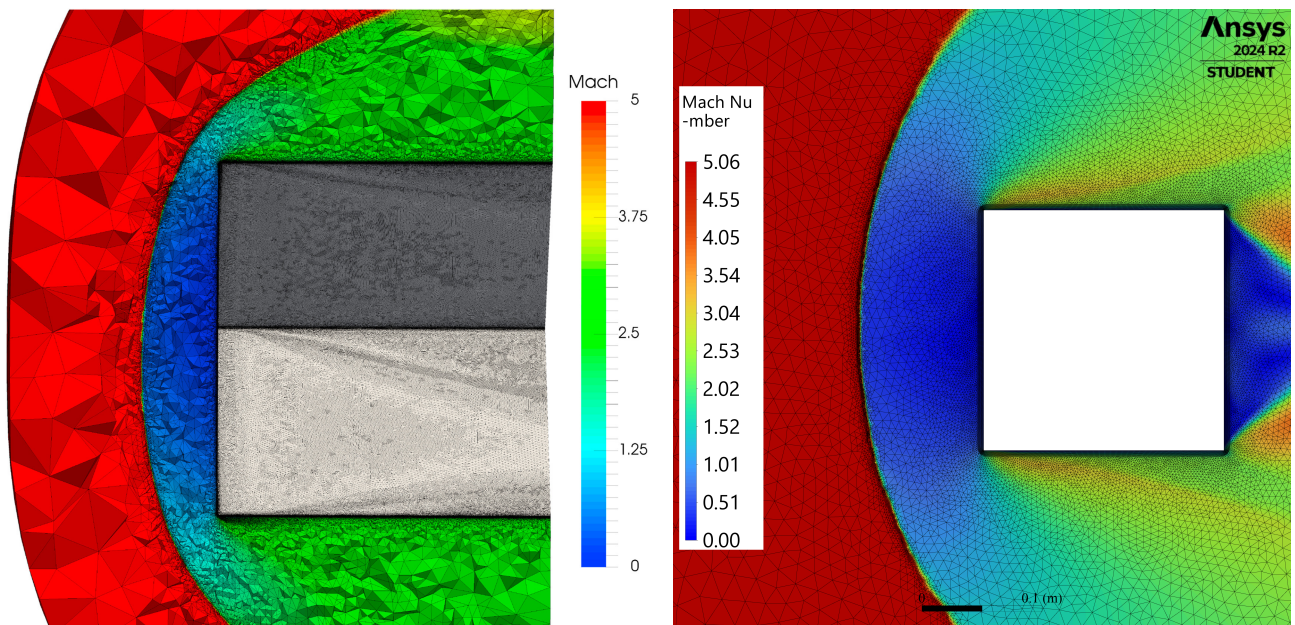


Figure 13: Comparison of Mach number contours between *Rees et al. (2021)* (left) and our Fluent Run 1 simulation (right). The results show good agreement. The standoff distance for the bow shock in our simulation is greater than that of Rees, which is consistent with the Fluent simulation running at a higher Reynolds number.

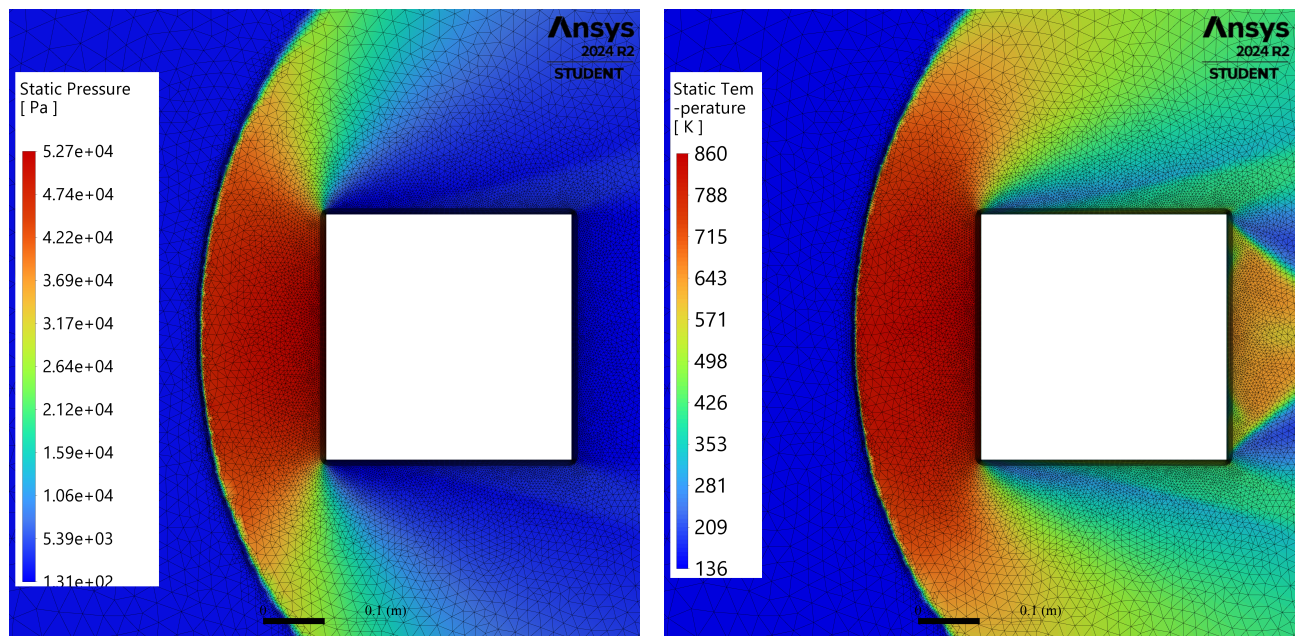


Figure 14: Run 1: static Pressure (left) and Temperature (right) distributions outputs of the CubeSat CFD simulation as contours of interpolated nodal values.

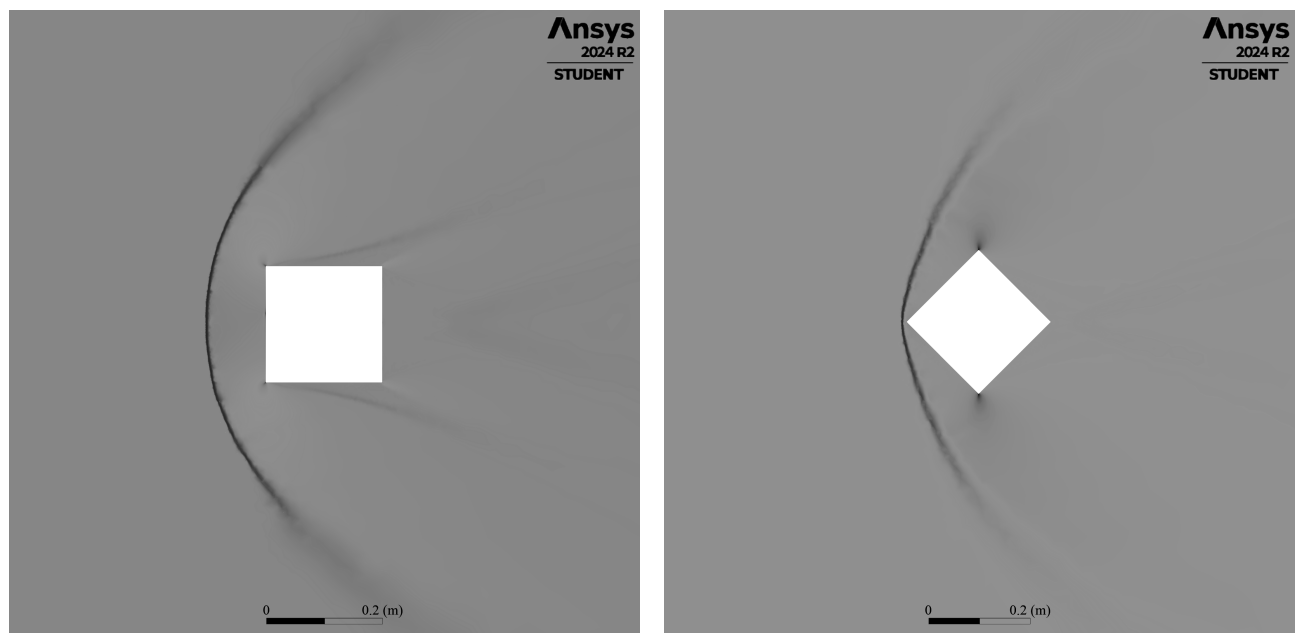


Figure 15: Schlieren (numerical) contours for Run 1 (left) and Run 2 (right). These flow distributions are a good qualitative match to Figure 6.

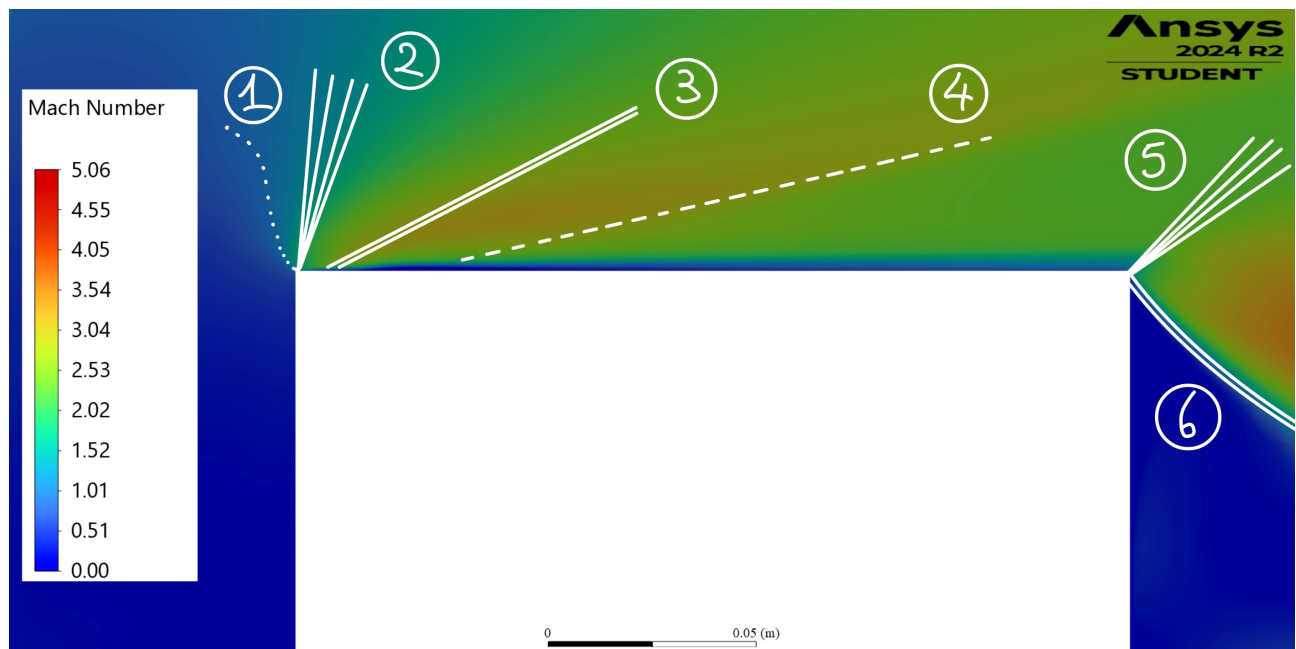


Figure 16: Detail of Mach number contours around the top half of the leading edge, top leeward edge and top half of the trailing edge. Flow structures show the presence of: ① Sonic Line, ② Leading-Edge Expansion Fan, ③ Re-Attachment Shock, ④ Weak Compression Wave, ⑤ Trailing-Edge Expansion Fan, ⑥ Wake Shock. These are consistent with the results of *Seltner, Willems, and GÜLhan (2019)* of Figure 6 (left).

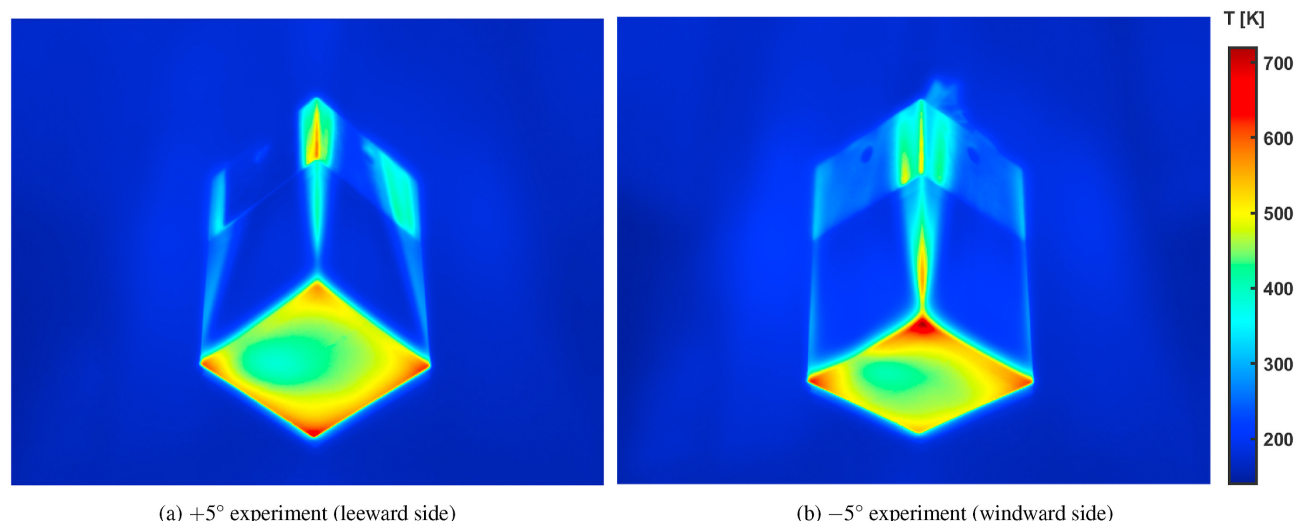


Figure 17: Experimental results of a Cube in Mach 5 flow at 5° incidence performed at the University of Manchester's High SuperSonic Tunnel (HSST). Experiment and figure by *Rees et al. (2020)*. The authors found that incidence had little influence over the maximum static temperature obtained at the corners. The experimental results are used to validate our predictions of Figure 14 (right).

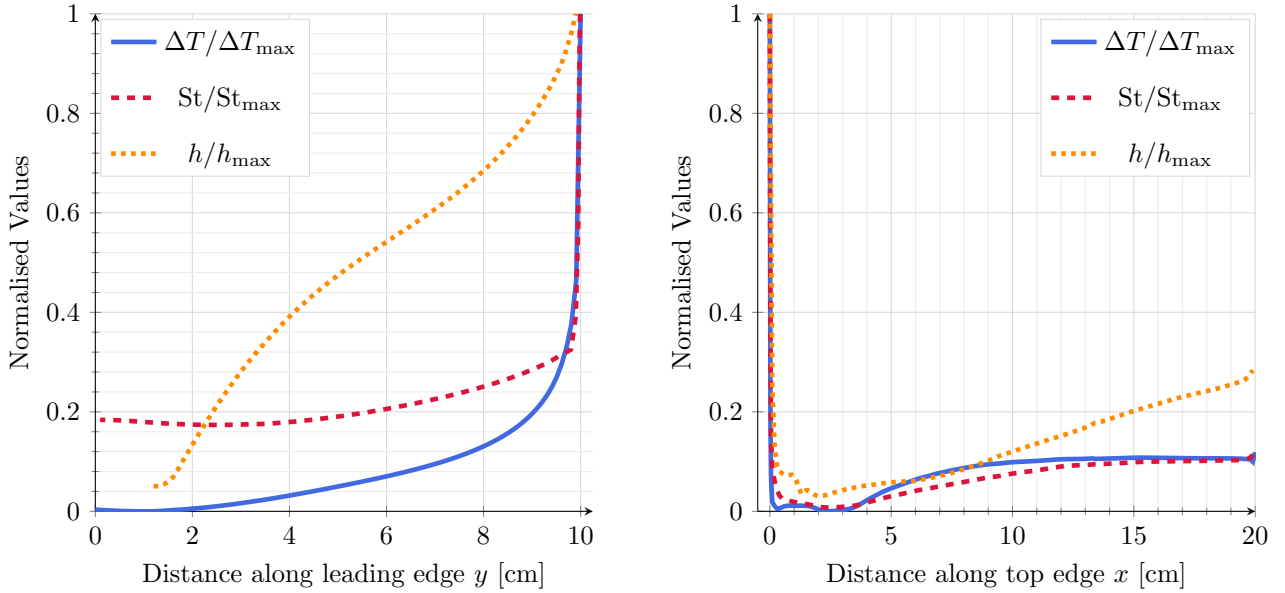


Figure 18: Run 1: Normalised temperature increase above stagnation point temperature, normalised Stanton number, and normalised y^+ -based heat transfer coefficient along the leading (frontal) edge (left); Normalised static temperature increase above minimum static temperature, normalised Stanton number, and normalised y^+ -based heat transfer coefficient along the leeward (top) edge (right).

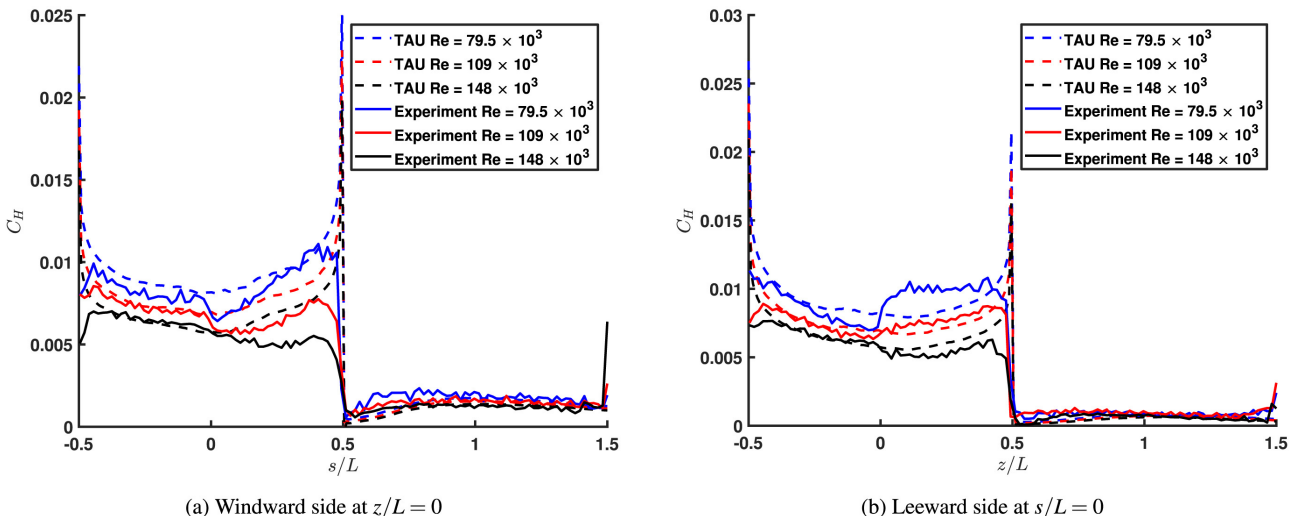


Figure 19: Stanton number distribution along the central cross section on the windward side (a) and leeward side (b) from both experimental and numerical sources. Experiments, simulations and figures by [25].

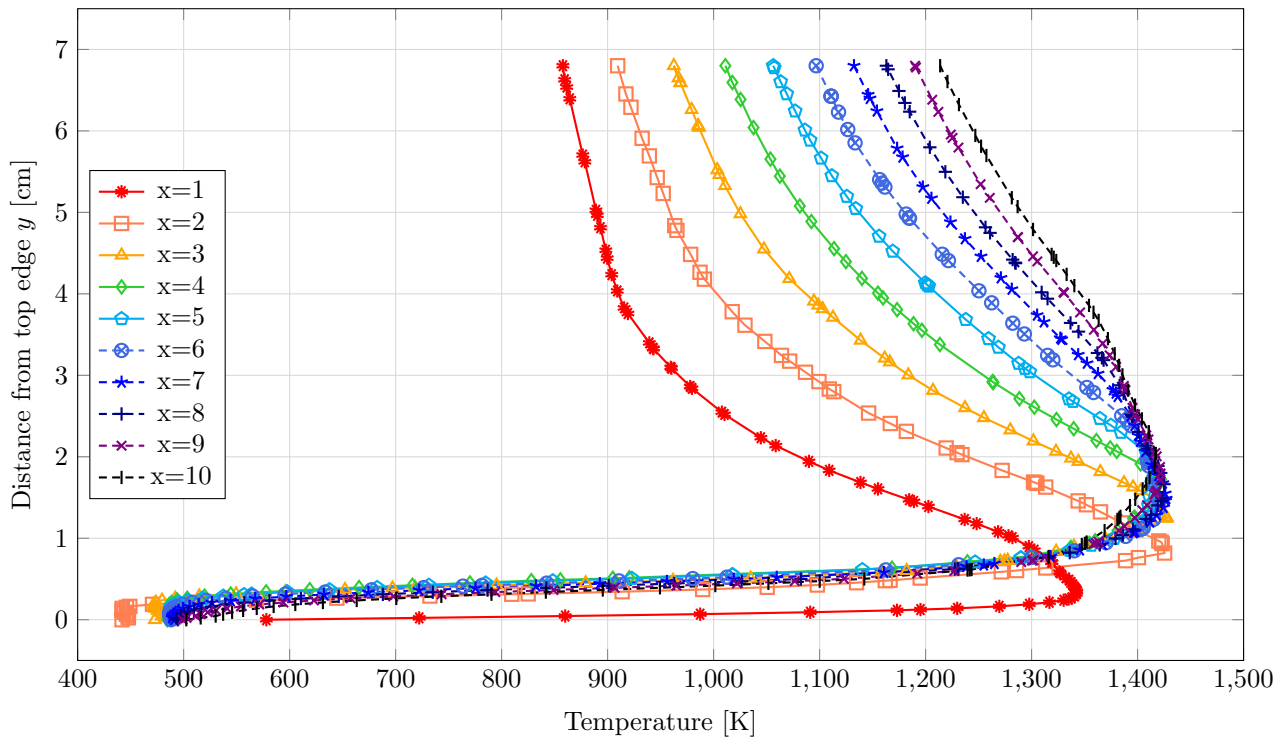


Figure 20: Run 3: temperature profiles within the viscous boundary layer at different streamwise positions (x -values, in cm) along the first half of the leeward (top) edge of the CubeSat. Surface temperature is found to lie between 400 K and 600 K, with the highest surface temperature just after the frontal corner Prantl-Meyer expansion.

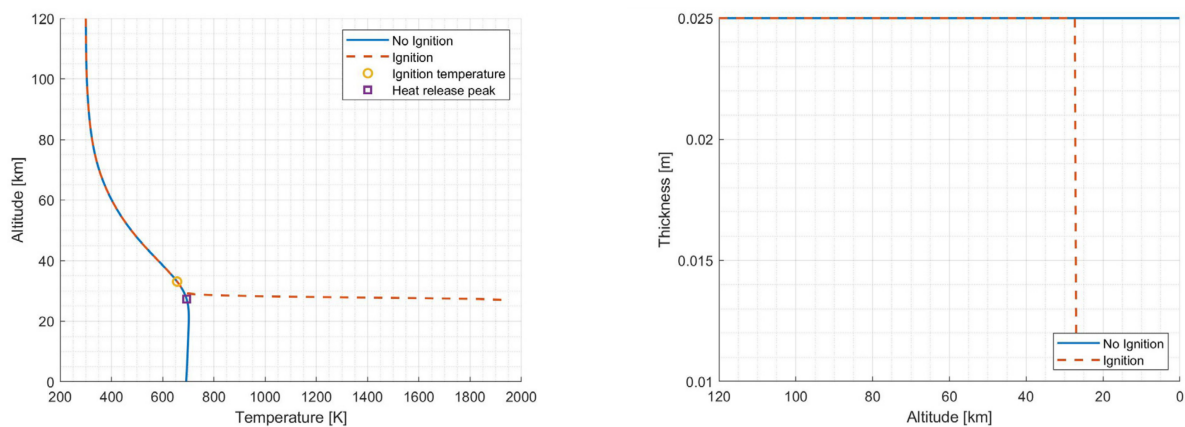


Figure 21: From Finazzi et al. (2024).